Lactiplantibacillus plantarum PS128 restores microbiota-driven polyamine homeostasis to alleviate autism-like behaviors in *Fmr1* knockout mice

Yingmin Cui[1, 5], Yingxuan Chen[1, 5], Yen-Wenn Liu[2, 5], Shan Zheng[1], Jialong Cui[3], Tianan Li[1], Ying-Chieh Tsai[2], Shanshan Gu[4], Ji Ma[1], Wei Zhang[1], Haipeng Li[4], Xiao-Bing Yuan[1, *], Yi-Hsuan Pan[1, 6, *]

[1]Key Laboratory of Brain Functional Genomics of Shanghai and Ministry of Education, Institute of Brain Functional Genomics, School of Life Science and the Collaborative Innovation Center for Brain Science, East China Normal University, Shanghai 200062, China

[2]Institute of Biochemistry and Molecular Biology, National Yang Ming Chiao Tung University, Taipei 11221, Taiwan

[3]Institute of Mechanobiology and Medical Engineering, School of Life Sciences and Biotechnology, Shanghai Jiao Tong University, Shanghai 201100, China

[4]Shanghai Institute of Nutrition and Health, University of Chinese Academy of Sciences, Chinese Academy of Sciences, Shanghai 200031, China.

[5]These authors contributed equally

[6]Lead contact

*Correspondence: yxpan@sat.ecnu.edu.cn (Y.H.P.), xbyuan@brain.ecnu.edu.cn (X.B.Y.)

Abstract

Background Autism spectrum disorder (ASD) is biologically heterogeneous and has limited mechanism-informed interventions targeting core behavioral symptoms. Emerging evidence suggests that gut microbial metabolism shapes neurobehavioral outcomes, yet the specific metabolic pathways linking gut ecology to brain function remain incompletely understood. One candidate pathway is polyamine metabolism, which links microbial amino acid metabolism to host regulation and represents a plausible but underexplored contributor to ASD-related phenotypes. Notably, the psychobiotic *Lactiplantibacillus plantarum* PS128 has been reported to improve social behaviors in individuals with ASD, although the molecular basis for these effects is unclear. In this study, we used Fragile X mental retardation 1 knockout (*Fmr1* KO) mice, a well-established ASD model, to investigate microbiota-dependent metabolic mechanisms underlying autism-like behaviors.

Results We found that autism-like behaviors in *Fmr1* KO mice were associated with gut dysbiosis, impaired intestinal barrier integrity, disruption of the arginine–ornithine–polyamine pathway, and elevated putrescine in the prefrontal cortex (PFC). Supplementation with PS128 remodeled the gut microbiota, reduced inflammation- and disease-associated taxa, improved intestinal structure and permeability, and restored polyamine homeostasis. Targeted metabolomics revealed an increased PFC-to-serum putrescine ratio in KO mice, which was normalized following PS128 intervention. This correction was accompanied by reduced expression of polyamine transporters in the PFC, including ATP13A family members. Causal experiments supported a functional role for putrescine, as peripheral elevation of putrescine induced autism-like behaviors in wild-type mice, whereas pharmacological inhibition of putrescine synthesis ameliorated behavioral deficits in *Fmr1* KO mice.

Conclusions These findings identify putrescine metabolic dysregulation as a key contributor to autism-like phenotypes and support the existence of an ASD subtype defined by disruption of the

arginine–ornithine–polyamine axis. Integrated multi-omics and causal perturbation analyses support a model in which microbiota-targeted intervention rebalances systemic polyamine regulation along the gut–brain axis, thereby improving ASD-relevant behaviors. Our work provides mechanistic evidence linking microbial metabolism to neurochemical homeostasis and highlights the translational potential of metabolic stratification in ASD.

Keywords Gut microbiota–metabolite–brain axis; polyamine; Fragile X mental retardation 1; prefrontal cortex.

Background

Autism spectrum disorder (ASD) encompasses a group of neurodevelopmental conditions characterized by deficits in social interaction and communication, accompanied by repetitive and restricted behaviors and interests. Both genetic and environmental factors contribute to ASD, with genetic influences playing a predominant role [1]. In recent years, ASD has emerged as a major public health concern due to its rising global prevalence [2, 3]. However, effective therapies targeting the core symptoms of ASD remain limited [4]. Growing evidence implicates metabolic disturbances in ASD pathophysiology, particularly involving amino acid metabolism, including branched-chain amino acids (BCAAs), arginine, and ornithine [5-8].

Microbial metabolites are increasingly recognized as key modulators of host physiology, with several shown to influence brain function through the gut–brain axis [9, 10]. Among the diverse classes of host- and microbiota-derived metabolites, putrescine is a polyamine primarily derived from arginine and ornithine catabolism. Putrescine interacts electrostatically with nucleic acids, proteins, lipids, and proteoglycans, thereby regulating gene expression, oxidative stress, cell proliferation, and inflammation [11]. Polyamine homeostasis is tightly regulated, and the intestinal microbiota represents a major exogenous source [12]. Notably, elevated levels of putrescine and its derivative spermine have been detected in the saliva of children with ASD [13], supporting a potential contribution of polyamine imbalance to ASD pathophysiology.

Probiotics, particularly psychobiotics, have attracted increasing interest as safe and accessible interventions capable of reshaping the gut microbiome and modulating neurobehavioral outcomes [14]. Clinical evidence indicates that daily supplementation with *Lactiplantibacillus plantarum* PS128 (PS128) has been associated with improvements in social behaviors and attention-related symptoms in individuals with ASD, with minimal adverse effects [15, 16]. However, the molecular pathways through which PS128 acts along the gut–brain axis to ameliorate ASD symptoms remain poorly defined. Fragile X mental retardation protein (FMRP), an RNA-binding protein encoded by the *Fmr1* gene, represents the most common monogenic cause of ASD [17], and its deficiency leads to both gastrointestinal and behavioral abnormalities in humans and mice [18, 19]. Accordingly, the *Fmr1* knockout (KO) mouse [20] provides a well-established model for dissecting gut–brain interactions in ASD and for uncovering the molecular mechanisms by which microbiota-targeted interventions may exert biological effects.

In this study, we investigated whether microbiota-targeted intervention can ameliorate autism-like phenotypes in *Fmr1* knockout mice. We identified disruption of the arginine–ornithine–polyamine metabolic pathway in the gut of KO mice and found that intervention with *Lactiplantibacillus plantarum* PS128 reshaped the gut microbiota and rebalanced peripheral–central putrescine homeostasis. This effect was accompanied by enrichment of beneficial bacterial taxa and suppression of inflammation- and disease-associated taxa in the gut, together with reduced expression of putrescine transporters in the prefrontal cortex (PFC). Furthermore, bidirectional manipulation of putrescine levels demonstrated a causal contribution of putrescine to autism-like phenotypes. These findings suggest putrescine as a candidate metabolic biomarker and therapeutic target for ASD.

Results

Microbiota-targeted intervention alleviates autism-like behaviors in *Fmr1* KO mice

To determine whether microbiota modulation mitigates behavioral abnormalities in *Fmr1* knockout (KO) mice, KO mice and their wild-type (WT) littermates received PS128-containing jelly every other day through voluntary oral consumption (Video S1). Behavioral performance was assessed using a comprehensive battery, including the open-field test (OFT), elevated plus maze (EPM), O-maze test (OMT), novel object recognition test (NORT), reciprocal social interaction test (RSIT), balance beam test (BBT), olfactory habituation/dishabituation test (OHDT), and tube test (TT) throughout the treatment period. These assays were selected to capture ASD-relevant behavioral domains, including anxiety-related behavior, repetitive and stereotypic behaviors, social interaction and novelty preference, and motor coordination.

Across most behavioral assays, PS128 intervention had minimal effects on WT mice (Figs. 1 and S1), and the behavioral alterations were primarily observed in *Fmr1* KO mice. In the OFT (Figs. 1A and S1A), KO mice exhibited significantly reduced total and central exploration distances compared with WT controls (Fig. 1B and 1C), indicating increased anxiety-like behavior. Following intervention, these measures were restored toward WT levels (Fig. 1A–1C), and time spent in the center zone increased (Fig. S1B and S1C), indicating attenuation of anxiety-like behavior in KO mice. No significant differences were detected in the EPM or OMT (Fig. S1D–S1I), suggesting that anxiety-related abnormalities in KO mice are context dependent.

In the NORT (Fig. 1D), KO mice showed a reduced recognition index (Fig. 1E) and excessive climbing on both familiar and novel objects (Fig. 1F), reflecting repetitive and stereotypic behaviors [21]. Similar repetitive climbing behavior was also observed in the OHDT (Fig. S1J–S1N, Videos S2 and S3), where KO mice frequently climbed and remained on the swab (Fig. S1J). Following intervention, both recognition deficits and stereotypic behaviors were ameliorated, with the recognition index restored toward WT levels and a marked reduction in excessive climbing.

In the RSIT (Fig. 1G), WT and WTPS mice displayed comparable interaction patterns (Fig. S1O). WT mice preferentially interacted with a novel mouse (Stage 3) over a familiar one (Stage 2), whereas KO mice did not (Fig. 1H and 1I), indicating impaired social novelty preference.

Intervention significantly improved social novelty preference and recognition performance in KO mice (Fig. 1D–1I).

In the BBT (Fig. 1J), KO mice required more time to traverse both 30° and 60° beams (Fig. 1K and 1L), indicating impaired motor coordination. Traversal performance was improved following intervention in KO mice, although performance did not fully reach WT levels. In the TT (Fig. S1P), PS128-treated KO mice exhibited a higher probability of forward movement against unfamiliar KO or WT opponents (Fig. S1Q and S1R), suggesting enhanced social confidence. Collectively, microbiota-targeted intervention robustly improved core autism-like phenotypes in *Fmr1* KO mice (Figs. 1 and S1).

Microbiota remodeling reduces inflammation- and disease-associated taxa in *Fmr1* KO mice

To characterize microbiota remodeling associated with behavioral improvement in *Fmr1* KO mice, we performed 16S rRNA sequencing and metagenomic profiling on fecal samples, together with fluorescence imaging of gut tissues, collected from KO mice and WT littermates before and during microbiota-intervention with PS128.

Before PS128 supplementation, 1-month-old KO mice (KO-1M) exhibited lower α-diversity than age-matched WT littermates (WT-1M) (Fig. 2A and 2B) and a distinct β-diversity profile (Fig. 2C). WT-1M mice harbored several beneficial genera, including *Bifidobacterium*, *Anaerostipes*, and *Blautia* (Fig. 2D), which are known to promote mucus secretion, protect against enteric pathogens, and modulate mucosal immunity [22]. In contrast, KO-1M mice displayed increased abundances of *Helicobacter* and *Chlamydia* (Fig. 2D), pathogenic taxa previously associated with gastrointestinal inflammation and neurobehavioral abnormalities [23, 24].

By four months of age, KO mice (KO-4M) maintained reduced α-diversity (Fig. S2A and S2B) and distinct β-diversity relative to WT-4M mice (Fig. 2E), along with persistently elevated *Helicobacter* and *Chlamydia* (Fig. 2F). Spearman correlation analysis further revealed that higher abundances of these taxa were associated with more severe behavioral deficits in KO-4M mice (Fig. 2G), including reduced social interaction time (RSIT), prolonged traversal latency (BBT), and impaired tube test (TT) performance.

To enable in vivo tracking, CFDA/SE-labeled PS128 was first validated for growth and tolerance to simulated gastric and intestinal fluids and showed no detectable differences from unlabeled bacteria (Fig. S3A–S3C). Fluorescence imaging revealed preferential retention and colonization of the administered strain (PS128) in the cecum and colon of both WT and KO mice (Figs. 2H–2J and S3), as well as in the stomach and small intestine of WT mice (Fig. S3D, S3F, and S3N). Independently, analysis of fecal samples from mice receiving unlabeled PS128 supplementation demonstrated pronounced microbiota remodeling (Figs. 2K, 2L, and S2C–S2E). Following intervention, KO mice (KOPS-4M) exhibited α-diversity comparable to WT-4M littermates (Fig. S2F and S2G) and a distinct β-diversity profile relative to untreated KO-4M mice (Fig. 2M). At the taxonomic level, KOPS-4M mice showed enrichment of *Lactiplantibacillus* and *Bifidobacterium*, together with reductions in *Ileibacterium*, *Enterorhabdus*, *Helicobacter*, and *Chlamydia* (Figs. 2K, 2L, 2N–2P and S2H–S2M). Overall, these results demonstrate that microbiota-targeted intervention with PS128 robustly reshapes gut microbial community structure

in *Fmr1* KO mice by reducing inflammation- and disease-associated taxa while enriching commensal genera, including *Lactiplantibacillus* and *Bifidobacterium*, in parallel with behavioral improvement (Figs. 2 and S2).

Restoration of gut barrier integrity accompanies microbiota remodeling

To determine whether microbiota remodeling was associated with restoration of intestinal structure and function, we performed anatomical, histological, and physiological analyses, using WT littermates as references.

KO mice displayed significantly elevated intestinal permeability in the intestinal permeability assay (IPA), which was attenuated following microbiota-targeted intervention with PS128 (Fig. 3A and 3B). In addition, KO mice exhibited pronounced gastrointestinal abnormalities, including elongation of the cecum and colon (Fig. 3C–3E), distorted crypt architecture (Fig. 3F and 3G), and reduced goblet cell numbers (Fig. 3H–3J), as well as diminished MUC2-positive areas (Fig. 3K–3M). This intervention alleviated these abnormalities, partially restoring mucosal architecture and improving epithelial barrier integrity. Collectively, these results demonstrate that microbiota-targeted intervention with PS128 substantially improves intestinal barrier structure and function in *Fmr1* KO mice.

Modulation of the gut arginine–ornithine–polyamine pathway by microbiota-targeted intervention with *Lactiplantibacillus plantarum* PS128

To investigate the functional consequences of microbiota remodeling on gut metabolic pathways, we reanalyzed the metagenomic datasets and performed whole-genome sequencing of the administered strain (PS128) to assess its microbial metabolic potential in *Fmr1* KO mice.

Based on KEGG annotation, microbial functions in KO mice were primarily enriched in carbohydrate and amino acid metabolism (Fig. S4A). Among these categories, amino acid metabolism showed the most pronounced difference between KO and WT mice, with the highest LDA score ($\log_{10} = 3.55$) (Fig. S4B). Microbiota-targeted intervention with PS128 further enhanced amino acid–related pathways in KO mice (Fig. S4C). These results highlight amino acid metabolic dysregulation as a prominent microbial feature associated with *Fmr1* deficiency and likely linked to physiological abnormalities.

We next reconstructed metagenome-assembled genomes (MAGs) by binning contigs derived from the metagenomic datasets [25] and identified gut–brain modules (GBMs) encoded by species-level genome bins (SGBs) (Fig. 4A). GBMs were categorized into eight functional clusters according to their relevance to gut–brain metabolic pathways. Among these, "Neurotransmitter metabolism I" (glutamate metabolism), "Amino acid metabolism II" (serine metabolism), and "Amino acid metabolism I" (arginine metabolism) contained the largest numbers of modules. Notably, "Amino acid metabolism I" showed the clearest difference between WT and KO mice and exhibited the most substantial recovery following microbiota-targeted intervention (Fig. 4B).

Proteins encoded by bins within "Amino acid metabolism I" were annotated and quantified (Fig. 4C), and highly expressed proteins were visualized using radar plots (Fig. 4D). Compared with WT littermates, KO mice displayed reduced abundance of spermidine/putrescine transport ATP-

204 binding and substrate-binding proteins, along with elevated levels of N-carbamoyl-putrescine
205 amidase, indicating diminished bacterial uptake and increased microbial production of putrescine.
206 KO mice also showed increased arginine decarboxylase and decreased ornithine
207 carbamoyltransferase, reflecting upstream disruption of arginine and ornithine metabolism.
208 Microbiota-targeted intervention with PS128 normalized these protein expression patterns,
209 resulting in a more balanced amino acid and polyamine metabolic profile in KOPS mice (Fig. 4D).
210 Whole-genome sequencing of PS128 revealed genes involved in arginine biosynthesis and
211 export, as well as in the uptake and degradation of spermidine and putrescine, whereas genes
212 required for de novo polyamine biosynthesis were absent (Fig. 4E). This genomic profile is
213 consistent with a putrescine-consuming role for PS128 in KO mice. In addition, functional
214 annotation showed that PS128-enriched taxa, including *Lactiplantibacillus plantarum*,
215 *Lactiplantibacillus paraplantarum*, and *Levilactobacillus brevis*, together with the six most
216 abundant bacterial species, harbor complementary genetic capacities for arginine, ornithine, and
217 polyamine uptake, degradation, and synthesis (Fig. 4F). Taken together, these analyses define a
218 coordinated microbial network through which microbiota modulation following PS128
219 intervention shapes arginine–ornithine–polyamine metabolism in the gut of *Fmr1* KO mice.
220
221 **Peripheral–central putrescine imbalance is corrected by coordinated polyamine regulation**
222 Behavioral improvement in *Fmr1* KO mice was most prominent in prefrontal cortex (PFC)–
223 dependent social domains and striatum (STR)–associated repetitive behaviors (Figs. 1 and S1).
224 Given that these behavioral changes coincided with remodeling of gut arginine–ornithine–
225 polyamine metabolism (Figs. 4 and S4), we next examined whether peripheral metabolic
226 alterations were reflected in polyamine homeostasis within the PFC and STR. To this end, we
227 performed targeted metabolomic profiling of 40 neuroactive substances, seven short-chain fatty
228 acids (SCFAs), and four additional fatty acids in both brain regions (Tables S1 and S2).
229 Volcano plot analysis revealed a marked elevation of putrescine in the PFC of KO mice relative
230 to WT littermates (Fig. 5A), which was significantly reduced following intervention with PS128
231 (Fig. S5A). This effect was largely region specific, as putrescine levels in the STR showed only
232 modest group differences (Fig. S5B and S5C). No significant differences were detected among
233 groups for the 11 fatty acids measured in either brain region (Fig. S5D–S5G). Because putrescine
234 circulates systemically (Fig. 5B), we next quantified serum putrescine using targeted UHPLC–
235 MS/MS and calculated the PFC-to-serum ratio. KO mice exhibited a significantly elevated ratio
236 compared with WT controls (Fig. 5C), whereas intervention with PS128 largely normalized this
237 imbalance (Fig. 5D), indicating a coordinated adjustment of peripheral and central putrescine
238 distribution in *Fmr1* KO mice.
239 To explore molecular changes accompanying this adjustment (Fig. 5D), we performed single-
240 nucleus RNA sequencing (snRNA-seq) on PFC tissue from KO and WT mice with or without
241 PS128 treatment. Overall cell-type composition was not appreciably altered (Figs. 5E, 5F, and
242 S6A). However, transcriptomic analysis revealed a predominance of downregulated genes
243 following PS128 treatment (Fig. S6B). Downregulated genes were enriched for pathways related
244 to chromosome organization, glycoprotein metabolism, and macroautophagy (Fig. S6C), whereas

upregulated genes were associated with telomere organization and protein folding (Fig. S6D). Notably, pathways involved in polyamine transmembrane transport were selectively downregulated in PS128-treated KO mice (Fig. 5H).

These pathways included *Atp13a2*, *Atp13a3*, and *Atp13a4* (Fig. S6B and S6E), which encode mammalian P5B-type ATPases implicated in cellular polyamine handling. Reduced expression of ATP13A2 and ATP13A3 in PS128-treated KO mice (KOPS) was confirmed by Western blotting (Fig. 5I–5K). In addition, *Atp13a4*, which is enriched in astrocytes forming part of the blood–brain barrier (Fig. S6F), also exhibited reduced expression (Fig. S6G). These results indicate that microbiota-targeted intervention with PS128 downregulates polyamine transport–related pathways in the PFC while restoring peripheral–central putrescine equilibrium in *Fmr1* KO mice.

Bidirectional manipulation of putrescine metabolism modulates autism-like behaviors in mice

To determine whether perturbation of putrescine metabolism contributes to autism-like behaviors, we administered putrescine dihydrochloride intraperitoneally (200 mg/kg) to 2-month-old wild-type (WT) mice (Fig. 6A). Although this treatment did not raise putrescine levels in the prefrontal cortex (PFC) (Fig. S7A), it was sufficient to induce multiple autism-like behavioral abnormalities. Treated WT mice showed reduced total exploration distance, center exploration distance, and center exploration time in the open-field test (OFT) (Fig. 6B–6F), impaired social interaction in the reciprocal social interaction test (RSIT) (Fig. 6G), and prolonged traversal time on the 30° balance beam (Fig. 6H). These results indicate that elevated peripheral putrescine (Fig. S7B) is sufficient to induce autism-like behavioral phenotypes in WT mice.

We next examined whether reducing putrescine synthesis could ameliorate autism-like behaviors in *Fmr1* KO mice. To this end, we used α-difluoromethylornithine (DFMO), an irreversible inhibitor of ornithine decarboxylase (Fig. 6I). Intraperitoneal DFMO administration (500 mg/kg) significantly lowered PFC putrescine levels in both 1- and 2-month-old KO mice (Fig. 6J and 6K). DFMO had no significant effect on locomotor activity in the OFT (Fig. 6L and 6M); however, compared with 2-month-old KO mice, DFMO modestly reduced center exploration distance and time in 1-month-old KO mice (Fig. S7C–S7F), suggesting age-dependent effects on anxiety-like behavior. Despite this, DFMO treatment increased social interaction time in the RSIT (Figs. 6N and S7G) and shortened traversal time on the 30° beam during the first trial of the balance beam test (BBT) (Fig. 6O and 6P). Early DFMO intervention also improved performance on the 60° beam in KO mice (Fig. 6Q). Moreover, DFMO-treated KO mice exhibited tube test performance comparable to that of PS128-treated KO mice (KOPS) (Figs. 6R and S1R), achieving higher winning scores than untreated KO mice (Fig. 6S and 6T).

Altogether, these results demonstrate that elevated peripheral putrescine is sufficient to induce autism-like behaviors, whereas pharmacological suppression of putrescine production ameliorates these deficits, supporting a causal role for putrescine imbalance in behavioral abnormalities in *Fmr1* KO mice.

Discussion

In this study, we show that altered microbial composition and dysregulated arginine–ornithine–polyamine metabolism are closely linked to autism-like behaviors in *Fmr1* KO mice. Microbiota-targeted intervention with *Lactiplantibacillus plantarum* PS128 reshaped the gut microbiota, improved intestinal integrity, and rebalanced putrescine homeostasis across the gut–brain axis, in part through coordinated regulation of microbial metabolism and host transport systems. Our data identify putrescine as a microbiota-responsive modulator of behavioral abnormalities and suggest that correction of the microbiota–polyamine–brain axis can occur through an integrated microbial–metabolic–neuronal pathway. These findings provide a conceptual framework for metabolic stratification and psychobiotic-based interventions in autism spectrum disorder.

Autism spectrum disorder (ASD) has substantial etiologic and phenotypic heterogeneity [4]. Genetic and environmental factors converge on the microbiota–gut–brain axis, where altered microbial metabolism influences amino acid turnover, neurotransmitter synthesis, epithelial integrity, and immune signaling [26]. Consistent with previous reports, *Fmr1* KO mice in our study exhibited repetitive and restricted behaviors, social impairments, and motor coordination deficits. These behavioral abnormalities were accompanied by intestinal dysbiosis, barrier dysfunction, and metabolic imbalance. Together, these features mirror reports of altered amino acid, lipid, and xenobiotic metabolism in ASD [27], as well as evidence linking mucosal barrier disruption [20] and microbial metabolite shifts to behavioral phenotypes [28, 29].

Sustained microbiota-targeted intervention with *Lactiplantibacillus plantarum* PS128 (PS128) markedly alleviated autism-like behaviors in *Fmr1* KO mice. Intervention with PS128 reduced the elevated abundances of *Helicobacter* and *Chlamydia*, two taxa highly correlated with autism-like behaviors in untreated *Fmr1* KO mice, and restored beneficial genera, such as *Lactiplantibacillus* and *Bifidobacterium*. While modulation of microbial composition is an anticipated outcome of probiotic intervention, we then asked whether such changes were accompanied by improvements in intestinal architecture or barrier-related features. Consistent with this possibility, intervention with PS128 ameliorated gastrointestinal abnormalities and barrier-associated features, supporting the conclusion that stabilization of microbial ecology contributes to improved intestinal integrity [30]. In addition, intervention increased the abundance of *Lactiplantibacillus paraplantarum*, *Levilactobacillus brevis*, and *Bifidobacterium pseudolongum*. Notably, *Lactiplantibacillus paraplantarum* has been reported to improve diabetes-related gastrointestinal complications and exert anti-inflammatory effects [31, 32]. These observations support a psychobiotic mode of action in which microbiota-targeted intervention promotes gut microbial homeostasis and intestinal integrity [15, 16, 33].

Beyond compositional rearrangement, intervention produced a distinct functional correction centered on the arginine–ornithine–polyamine metabolic pathway. Among polyamines, putrescine occupies a unique position at the interface of gut microbial metabolism and host regulation, rendering it sensitive to microbiota-driven metabolic perturbations [34]. Because the administered strain (PS128) lacks de novo putrescine biosynthesis but encodes uptake and catabolic functions, it likely contributes to the regulation of systemic putrescine handling rather than serving as a

primary source of polyamine production. Consistent with this model, intervention with PS128 normalized the elevated prefrontal cortex (PFC)-to-serum putrescine ratio in *Fmr1* KO mice toward wild-type levels. This correction was accompanied by reduced expression of the polyamine transporters ATP13A2 and ATP13A3 in the PFC, together with decreased *Atp13a4* expression in astrocytes at the single-cell level in PS128-treated *Fmr1* KO mice. ATP13A2 and ATP13A3 are major determinants of mammalian polyamine uptake [35], and their downregulation is consistent with reduced prefrontal cortical accumulation of putrescine. Such coordinated changes suggest a homeostatic adjustment to altered polyamine availability, in line with their established roles in mammalian polyamine transport and cellular polyamine balance. Mutations or dysfunction in these transporters have been associated with ASD and related neurodevelopmental conditions [36-39]. These observations link microbial activity to central polyamine handling and support a model in which microbiota-targeted intervention modulates gut-derived putrescine flux and neuronal transporter expression.

We identify putrescine as a microbiota-sensitive regulator of autism-like behaviors. Elevating peripheral putrescine was sufficient to induce anxiety-like behaviors, social impairments, and motor deficits in wild-type mice, whereas inhibition of endogenous putrescine synthesis with DFMO ameliorated these abnormalities in *Fmr1* KO mice. At physiological pH, putrescine carries a positive charge and interacts with nucleic acids, phospholipids, and anionic proteins, thereby influencing macromolecular conformation, autophagy, membrane dynamics, and inflammatory signaling. Altered polyamine handling, including astrocytic uptake via ATP13A4, has been shown to modulate excitatory synaptic transmission and neuronal physiology [40]. Because putrescine serves as a metabolic precursor for astrocyte-derived γ-aminobutyric acid (GABA) through a noncanonical MAO-B- and ALDH-dependent pathway [41], perturbations in putrescine availability may reshape inhibitory tone and excitation–inhibition balance in cortical circuits. Clinical observations of elevated salivary putrescine [13] and increased activity of the gut microbial arginine–polyamine program in children with ASD [42] further support the concept that putrescine delineates a metabolically defined ASD subtype that may be preferentially responsive to microbiota-targeted interventions.

In our study, initiating DFMO at four weeks of age raised safety considerations, as juvenile *Fmr1* KO mice already exhibited mild anxiety-like behaviors. These results suggest that early inhibition of endogenous putrescine synthesis may exert age-dependent adverse effects on emotional regulation. Across behavioral endpoints, microbiota-targeted intervention produced broader and more consistent behavioral improvements than DFMO, consistent with its dual ecological (microbiota restructuring) and metabolic (polyamine modulation) actions.

Probiotic-based approaches are increasingly recognized as safe, non-pharmacological options for neurological and psychiatric disorders [43, 44]. *Lactobacillus reuteri* restored social behavior through vagus-dependent oxytocinergic and dopaminergic signaling [45]. The microbial metabolite 5-aminovaleric acid improved autism-like behaviors in BTBR mice by reducing pyramidal neuron excitability in the PFC [29]. *Bacteroides uniformis* reinstated excitation–inhibition balance in *Chd8*$^{+/-}$ mice by modulating intestinal amino acid transport and reducing

prefrontal glutamine levels [46]. In a valproic acid–induced ASD mouse model, PS128 ameliorated social and memory deficits by enhancing oxytocin signaling and increasing dendritic complexity in the hippocampus and PFC [47]. Collectively, these studies support a framework in which psychobiotics influence brain function through coordinated effects on microbial metabolites, host transport systems, and cortical circuit activity. Because metabolic abnormalities have been widely reported in ASD across multiple metabolomics studies, future diagnostic strategies may complement current behavior-based assessments (e.g., DSM-5-TR) with metabolite-informed stratification.

This study has several limitations. We relied on a single genetic model, which limits the generalizability of our findings to other ASD subtypes. Although our multi-omics analyses support a gut-driven influence on polyamine homeostasis, the specific contributions of individual transporters and brain cell types remain to be delineated. Future studies incorporating transporter-specific perturbations, isotope-labeled tracing of gut-to-brain polyamine flux, and in vivo circuit-level measurements during behavior will help clarify mechanistic causality. Clinical translation will also require longitudinal studies integrating microbiome, metabolomic, and behavioral profiling in human cohorts. Ultimately, microbiota-targeted interventions may be combined with pharmacological or behavioral approaches and tailored to baseline metabolic phenotypes, enabling precision treatment strategies for ASD subtypes characterized by disrupted arginine–ornithine–polyamine metabolism.

Conclusion

Our findings identify putrescine as a candidate metabolic marker for an ASD subtype and support a model in which *Lactiplantibacillus plantarum* PS128 modulates gut-derived polyamine metabolism and central polyamine transporter expression, thereby driving robust improvements in social and stereotypic behaviors.

Methods

Animals and Ethical Statement

Female C57BL/6J mice were obtained from Shanghai Jihui Laboratory Animal Care Co., Ltd. (Cat# SHJH-M-01002), and male *Fmr1* knockout (KO) mice (RRID: IMSR_JAX:004624) were obtained from The Jackson Laboratory. To generate *Fmr1* KO mice on a uniform C57BL/6J genetic background, the KO line was backcrossed with wild-type C57BL/6J mice for ten generations. Male wild-type and *Fmr1* KO littermates on a C57BL/6J background were used for all experiments. Mice were housed in groups of six under specific pathogen-free (SPF) conditions at the multifunctional platform for innovation (Platform 101). The animal facility was maintained at 22 ± 1°C and 50 ± 5% relative humidity under a twelve-hour light/twelve-hour dark cycle (lights on at 6:00 a.m. and off at 6:00 p.m.). All mice had ad libitum access to water and a standard chow diet, with daily food intake set at 2.5 g per mouse from 1 month of age and 3.0 g per mouse from 2 months of age onward.

405 **Bacterial Strains and Growth Conditions**
406 *Lactiplantibacillus plantarum* PS128 was obtained from Centro Sperimentale del Latte Srl (Cat#
407 G001723) and cultured in de Man-Rogosa-Sharpe (MRS) broth (Solarbio, Cat# M8540) at 37ºC
408 for liquid cultures or on MRS agar plates supplemented with 1.5% (w/v) agar (Sangon Biotech,
409 Cat# A505255-0250).
410
411 **Preparation of Jelly Enriched with PS128, Blank Controls, and FITC**
412 Gelatin-based jellies were prepared as follows. Briefly, 2.1 g of gelatin (Sinopharm, Cat#
413 10010326) and 0.3 g of sucrose (Sigma, Cat# V900116) were dissolved in 22.5 mL of sterilized
414 double-distilled water (ddH_2O) by heating to 55ºC under constant stirring. The solution was then
415 diluted with sterilized ddH_2O prewarmed to 55ºC to a final volume of 30 mL while continuously
416 stirred.
417 The gelatin solution was evenly divided into two sterilized glass beakers and one 50-mL
418 centrifuge tube (10 mL each) and maintained at 37ºC. Lyophilized *Lactiplantibacillus plantarum*
419 PS128 (0.46 g) was added to one beaker, and fluorescein isothiocyanate (FITC)–dextran (0.6 g,
420 Aladdin, Cat# F121152) was added to the centrifuge tube. All procedures involving FITC were
421 performed under light-protected conditions. Both beakers were placed on magnetic stirrers in a
422 laminar-flow hood, whereas the centrifuge tube was mixed using a Genie 2 vortex mixer until fully
423 homogenized. Aliquots of 150 μL from the PS128-enriched and blank gelatin solutions and 300
424 μL from the FITC–dextran solution were dispensed into sterilized custom-made 0.5-mL jelly
425 molds. The molds (0.9 cm in diameter and 1.2 cm in height) were generated by trimming the upper
426 portion of 2-mL cryogenic vials with conical round bottoms. The filled molds were incubated at
427 4ºC for 2 hours to allow complete gelation.
428 After solidification, jellies were removed from the molds using sterilized tweezers. Each mouse
429 was provided with one PS128-enriched jelly containing approximately 2.07×10^9 colony-forming
430 units (CFU) of *Lactiplantibacillus plantarum* PS128 once every two days. FITC-enriched jellies
431 were prepared fresh as needed, and each mouse was provided with one jelly delivering 0.018 g of
432 FITC–dextran per 30-g body weight.
433
434 **Training Mice for Voluntary Jelly Intake**
435 Male wild-type (WT) and *Fmr1* knockout (KO) littermates at 3 weeks of age were housed
436 separately for 1 week and then randomly assigned to four groups: WT, WTPS, KO, and KOPS.
437 Mice in the WTPS and KOPS groups were provided with one PS128-enriched jelly every two days,
438 whereas mice in the WT and KO groups were provided with one blank jelly on the same schedule
439 (Video S1). To facilitate recognition and voluntary consumption of the jelly, the jelly surface was
440 lightly coated with powdered standard chow during the first three feeding sessions.
441
442 **Behavioral Experiments**
443 Behavioral testing was initiated after 28 consecutive days of exposure to PS128-enriched jelly or
444 blank jelly. All tests were conducted between 9:00 a.m. and 3:00 p.m., with a minimum 2-day

interval between consecutive tests to minimize stress. Prior to behavioral assessment, mice were handled for 10 minutes per day for 3 consecutive days and acclimated to the testing room for 2 hours on the test day.

Behavioral assays were performed in the following order: open-field test, novel object recognition test, elevated plus maze test, O-maze test, reciprocal social interaction test, olfactory habituation/dishabituation test, tube test, and balance beam test. Mouse behavior during training and testing sessions was recorded using the ANY-maze behavioral tracking system (version 7.20) and/or video cameras. All apparatuses were cleaned with 35% ethanol between individual mice, and a 5-minute interval was allowed between sessions to dissipate residual odors. Detailed procedures for each behavioral test are provided in Supplementary Material 1.

Intestinal Permeability Assay

Four-month-old mice were fasted for 4 hours before actively consuming FITC–dextran–enriched jelly at a dose of 0.6 mg per g body weight. Four hours after jelly consumption, approximately 800 μL of venous blood was collected from each mouse via orbital blood sampling under isoflurane anesthesia and transferred to a 1.5-mL microcentrifuge tube. Blood samples were allowed to clot at 25ºC for 1 hour, followed by centrifugation at 3,000 rpm for 10 minutes. The supernatant was carefully transferred to a clean 1.5-mL microcentrifuge tube and centrifuged again at 12,000 rpm for 10 minutes at 4ºC.

A total of 200 μL of clarified serum was mixed with an equal volume of phosphate-buffered saline (PBS), and 150 μL of the diluted serum was added in duplicate to a 96-well flat-bottom black microplate. Fluorescence intensity of FITC–dextran in serum was measured using a spectrofluorometer at excitation and emission wavelengths of 485 nm and 528 nm, respectively. A standard curve was generated using serial dilutions of FITC–dextran in PBS (0, 1.0, 2.0, 4.0, and 6.0×10^{-4} μg/μL), and serum FITC–dextran concentrations were calculated by interpolation according to the manufacturer's instructions.

Histological Evaluation of Transverse Colon

Colon segments (1.5 cm in length, located 1.5–3.0 cm proximal to the distal colon) were excised and fixed in 4% paraformaldehyde in phosphate-buffered saline (PBS; pH 7.4) at 4ºC for 24 hours. After fixation, tissues were washed in PBS, dehydrated through a graded ethanol series, and embedded in paraffin. Paraffin-embedded samples were sectioned at a thickness of 5 μm and mounted onto adhesive microscope slides.

Sections were deparaffinized, rehydrated, and stained with hematoxylin and eosin (H&E, Beyotime, Cat# C0105S) or Alcian blue–periodic acid–Schiff (AB–PAS, Leagene, Cat# DG0007). Images were acquired using an LED-illuminated light microscope. For quantitative analysis, three consecutive intact crypts per section, defined as fully visible and undamaged structures, were randomly selected. Measurements were performed on at least three independent sections per mouse.

485 **Immunofluorescence Assay**
486 Paraffin-embedded sections were subjected to antigen retrieval by incubation in sodium citrate
487 buffer (10 mM, pH 6.0) at 99ºC for 15 minutes. Sections were then blocked in a solution containing
488 0.5% Triton X-100 (Sigma, Cat# T8787-100ML), 5% goat serum (Beyotime, Cat# C0265), and
489 5% bovine serum albumin (Sangon Biotech, Cat# A602440-0050) for 2 hours at room temperature.
490 After blocking, sections were incubated with a primary antibody against ZO-1 (1:200, Thermo
491 Fisher, Cat# ZO1-1A12) at 4ºC for 36 hours. Following rinsing in phosphate-buffered saline (PBS),
492 sections were incubated with an appropriate secondary antibody (1:500, Thermo Fisher, Cat# A-
493 11003) for 2 hours at 37ºC. Fluorescent signals were imaged using a confocal laser scanning
494 microscope with excitation and emission wavelengths of 557 nm and 572 nm, respectively.
495
496 **Treatment Protocols for DFMO and Putrescine**
497 α-Difluoromethylornithine (DFMO, MedChemExpress, Cat# HY-B0744) and putrescine
498 dihydrochloride (Sangon Biotech, Cat# A600793) were dissolved in sterile saline at room
499 temperature and administered via intraperitoneal injection (i.p.). For juvenile *Fmr1* knockout (KO)
500 mice, DFMO treatment was initiated at 4 weeks of age at a dose of 500 mg per kg body weight,
501 administered every other day for 28 days. After mice reached 2 months of age, DFMO
502 administration was continued throughout the behavioral testing period until tissue collection. For
503 adult mice, *Fmr1* KO mice received DFMO at a dose of 500 mg per kg body weight once daily
504 for 7 consecutive days, whereas adult wild-type (WT) mice received putrescine dihydrochloride
505 at a dose of 200 mg per kg body weight once daily for 7 consecutive days. Treatments were
506 maintained throughout behavioral testing until tissue collection.
507
508 **Determination of Putrescine in Prefrontal Cortex**
509 Following behavioral assessments, mice were euthanized under deep isoflurane anesthesia, and
510 the prefrontal cortex (PFC) was rapidly dissected and weighed. Tissue homogenates were prepared
511 by adding lysis buffer at a ratio of 500 μL per 0.1 g of tissue, followed by homogenization and
512 incubation on ice for 10 minutes. Homogenates were centrifuged at 12,000 rpm for 5 minutes at
513 4ºC, and the supernatant was collected for putrescine quantification.
514 Putrescine concentrations were measured using a commercial enzyme-linked immunosorbent
515 assay (ELISA) kit (Enzyme-linked, REF: YJ523211) according to the manufacturer's instructions.
516 Samples were diluted 1:5 in dilution buffer, and 50 μL of each diluted sample or standard was
517 added to pre-coated wells together with 100 μL of horseradish peroxidase (HRP)–conjugated
518 detection antibody. After incubation for 60 minutes at 37ºC, wells were washed five times,
519 followed by the addition of substrate solution and incubation in the dark for 15 minutes. The
520 reaction was terminated with stop solution, and absorbance was measured at 450 nm. Putrescine
521 concentrations were calculated from a standard curve and corrected for the dilution factor.
522
523 **Immunoblotting**

524 Prefrontal cortex tissues were homogenized individually in ice-cold lysis buffer supplemented with
525 a protease inhibitor cocktail [48]. Protein concentrations were determined, and 20 μg of total
526 protein per sample was loaded onto 10% SDS–polyacrylamide gels for electrophoretic separation,
527 followed by transfer onto 0.2-μm polyvinylidene difluoride (PVDF) membranes using an
528 electroblotting system.
529 The PVDF membranes were blocked in TBST blocking buffer for 16 hours at 4ºC, followed by
530 incubation overnight at 4ºC with primary antibodies: anti-ATP13A3 (1:500, Proteintech, Cat#
531 55108-1-AP), anti-ATP13A2 (1:200, Santa Cruz, Cat# sc-293367), and anti-β-actin (1:10000,
532 Santa Cruz, Cat# sc-47778).
533 Following three washes with TBST, the blots were incubated with goat anti-mouse IgG labeled
534 with horseradish peroxidase (HRP) (1:1000, Beyotime, Cat# A0216) or goat anti-rabbit IgG
535 labeled with HRP (1:1000, Beyotime, Cat# A0208) and visualized using a chemiluminescent HRP
536 detection kit (Millipore, Cat# WBKLS0500). Images of the blots were captured using the
537 ImageQuant LAS-4000 system, and the density of protein bands was quantified using ImageQuant
538 TL software (version 7.0). The relative protein quantity was determined by normalizing the density
539 of the target protein band to the density of the β-actin band in the same lane. Western blot analysis
540 included two or six technical replicates for each sample.
541
542 **Fluorescent Labeling of PS128**
543 Overnight cultures of *Lactiplantibacillus plantarum* PS128 were inoculated into sterile MRS broth
544 at a 1% (v/v) ratio and grown to an optical density at 600 nm (OD_{600}) of 1.0. Bacterial cells were
545 harvested by centrifugation at 5,000 × g for 2 minutes at 4ºC and washed three times with
546 phosphate-buffered saline (PBS). Carboxyfluorescein diacetate succinimidyl ester (CFDA/SE,
547 MedChemExpress, Cat# HY-D0938) was then added to a final concentration of 20 μM, and
548 bacteria were incubated in the dark at 37ºC for 30 minutes. Excess dye was removed by washing
549 the cells three times with PBS.
550 Following labeling, PS128 cells were resuspended in PBS at concentrations of 1×10^9 or $1 \times$
551 10^{10} colony-forming units (CFU) per milliliter. A small aliquot of the bacterial suspension was
552 mounted onto microscope slides, and fluorescence images were acquired using a fluorescence
553 microscope. Labeling efficiency was calculated as the proportion of fluorescently labeled cells
554 relative to the total number of cells. Quantification was performed by randomly selecting seven
555 fields of view from samples at 1×10^9 CFU/mL and three fields of view from samples at 1×10^{10}
556 CFU/mL.
557
558 **Determination of PS128 Growth Before and After CFDA/SE Treatment**
559 PS128 cultures at a concentration of 1×10^{10} colony-forming units (CFU) per milliliter, with or
560 without CFDA/SE labeling, were inoculated into sterile MRS broth at a 3% (v/v) ratio. Bacterial
561 growth was monitored by measuring the optical density at 600 nm (OD_{600}) every 30 minutes during
562 the first 2 hours and then every 1 hour up to 8 hours to generate growth curves. For each condition,

563 OD_{600} values at each time point were calculated as the mean of two technical replicates from five
564 independent bacterial cultures.
565
566 **Determination of PS128 Tolerance to Gastric and Intestinal Fluids**
567 Tolerance of *Lactiplantibacillus plantarum* PS128 to simulated gastric fluid (SGF, Phygene, Cat#
568 PH1840) and simulated intestinal fluid (SIF, Phygene, Cat# PH1841) was assessed based on
569 previously described methods by Corcoran et al. [49] and Azat et al. [50], with modifications.
570 Briefly, PS128 cells resuspended in phosphate-buffered saline (PBS) were collected by
571 centrifugation at 5,000 × g for 2 minutes at 4ºC and resuspended in 2.5 mL of MRS broth for a
572 recovery period of 2.5 hours.
573 An 800-µL aliquot of PS128 culture at a concentration of 1×10^{10} colony-forming units (CFU)
574 per milliliter was mixed with an equal volume of MRS broth (control), a 1:1 mixture of MRS broth
575 and SGF, or a 1:1 mixture of MRS broth and SIF. Cultures containing SGF were overlaid with
576 mineral oil (Acmec, Cat# M97740) to maintain anaerobic conditions and incubated statically for
577 3 hours, whereas cultures containing SIF were incubated with shaking at 160 rpm for 4 hours.
578 Cultures in MRS broth alone served as controls.
579 After incubation, 200 µL of each bacterial suspension at a 10^{-5} dilution was plated onto MRS
580 agar plates. Following incubation at 37ºC for 24 hours, colonies were imaged and counted using
581 ImageJ software (version 1.54f). Tolerance was calculated as the percentage of colony-forming
582 units recovered after SGF or SIF exposure relative to the MRS control. Six independent
583 experiments were performed for statistical analysis.
584
585 **Detection and relative quantification of PS128 in fecal samples**
586 Fresh fecal samples were collected from 3.5-month-old mice and incubated with lysozyme (3
587 mg/mL, Tiangen, Cat# RT401) in lysis buffer containing 10 mM Tris and 1 mM EDTA (pH 8.0,
588 Sangon Biotech, Cat# EB0185) at 30ºC for 5 minutes to facilitate bacterial cell lysis. Total RNA
589 was isolated using TRIzol reagent according to the manufacturer's instructions (TransGen Biotech,
590 Cat# ER501). Complementary DNA (cDNA) was synthesized using the FastKing RT kit (Tiangen,
591 Cat# KR116) following the manufacturer's protocol. A positive control was prepared using 3 mL
592 of PS128 culture at an optical density at OD_{600} of 0.6.
593 PS128-specific primers (Fig. S3V) for PCR and real-time reverse transcription quantitative PCR
594 (RT-*q*PCR) [51] were designed based on the complete PS128 genome generated in this study and
595 deposited in the NCBI database (BioProject accession number PRJNA1345344). PCR
596 amplification was performed using 2× Taq Plus Master Mix II (Vazyme, Cat# P213-02) with an
597 initial denaturation step at 94ºC for 3 minutes, followed by 40 cycles of denaturation at 94ºC for
598 30 seconds, annealing at 48ºC for 35 seconds, and extension at 72ºC for 25 seconds, with a final
599 extension at 72ºC for 10 minutes. Ten microliters of each PCR product were resolved on a 2%
600 agarose gel and visualized under ultraviolet illumination using a gel documentation system.
601 RT-*q*PCR was performed using SYBR Green Master Mix (Qiagen, Cat# 208054) on a CFX
602 Connect Real-Time PCR Detection System with 35 cycles consisting of denaturation at 95ºC for

603 5 seconds followed by annealing and extension at 60ºC for 30 seconds. Data were analyzed using
604 Bio-Rad CFX Maestro software (version 3.1.1517.0823). Relative PS128 abundance was
605 calculated using the $2^{-\Delta\Delta Ct}$ method, with bacterial 16S rRNA serving as the internal reference.

606 **Imaging the Localization of PS128 in the Mouse Gut**

607 Adult mice in the PS128 group were administered 500 μL of fluorescently labeled PS128 (1×10^{10}
608 CFU/mL) by oral gavage once daily for 3 consecutive days, whereas control mice received 500
609 μL of phosphate-buffered saline (PBS). After the final gavage, mice were divided into two groups
610 for analysis.

611 For the first group, mice were anesthetized with isoflurane, and the abdominal area was shaved
612 to facilitate in vivo fluorescence imaging using an IVIS Lumina III Smart Imaging System.
613 Following whole-body imaging, mice were euthanized by cervical dislocation under deep
614 isoflurane anesthesia, and the entire gastrointestinal tract was immediately isolated. Ex vivo
615 fluorescence imaging of the gut was performed using the IVIS system with an excitation
616 wavelength of 480 nm and an emission wavelength of 520 nm. Total and mean fluorescence
617 intensities within defined regions of interest were quantified using Living Image software (version
618 4.5.2).

619 For the second group, mice were euthanized immediately after the final gavage. Segments of
620 the gastrointestinal tract were collected, including a 10-cm segment of the small intestine proximal
621 to the stomach, the cecum, and a 1.5-cm segment of the distal colon near the anus. Tissues were
622 cut into approximately 5-mm squares and imaged using a stereoscopic fluorescence microscope.
623 Mean fluorescence intensity was quantified using ImageJ software.

624

625 **Whole-genome sequencing and annotation of *Lactiplantibacillus plantarum* PS128**

626 Whole-genome sequencing of *Lactiplantibacillus plantarum* PS128 was performed by BGI
627 Genomics Co., Ltd. (Shenzhen, China) using a hybrid sequencing strategy. Detailed protocols for
628 sequencing and annotation are provided in Supplementary Material 1. Whole-genome sequencing
629 data for PS128 have been deposited in the NCBI database (BioProject accession number
630 PRJNA1345344).

631

632 **16S rRNA Gene Sequencing and analysis**

633 DNA extraction, PCR amplification, library construction, and sequencing were performed by
634 Origin-gene Biotechnology Co., Ltd. (Shanghai, China). Fecal samples were collected from four
635 mouse groups (WT, WTPS, KO, and KOPS) at 8:00 p.m. Microbial genomic DNA was extracted
636 using the QIAamp Fast DNA Stool Mini Kit (Qiagen, Germany) and assessed by 1% agarose gel
637 electrophoresis. Comprehensive protocols for 16S rRNA gene sequencing and analysis are
638 provided in Supplementary Material 1. The 16S rRNA gene sequencing data have been deposited
639 in the NCBI Sequence Read Archive (BioProject accession number PRJNA1345244).

640

641 **Metagenomic Sequencing and Analysis**

642 ***Sample preparation and sequencing***

643 Total genomic DNA was extracted from 0.2 g of fecal sample using the MagAttract PowerSoil Pro
644 DNA Kit (Qiagen, Germany) according to the manufacturer's instructions. DNA concentration
645 and purity were measured using a Quantus Fluorometer (PicoGreen, Promega, USA) and a
646 NanoDrop 2000 spectrophotometer (Thermo Fisher Scientific, USA), respectively, and DNA
647 integrity was assessed by 1% agarose gel electrophoresis.
648 Extracted DNA was fragmented to an average size of approximately 350 bp using a Covaris
649 M220 Focused-ultrasonicator for paired-end library construction. Sequencing libraries were
650 prepared using the NEXTFLEX Rapid DNA-Seq Kit (Bioo Scientific, USA) following the
651 manufacturer's protocol and sequenced on an Illumina NovaSeq 6000 platform (S4 flow cell).
652 DNA extraction, library construction, and sequencing were performed by Majorbio Bio-Pharm
653 Technology Co., Ltd. (Shanghai, China). Full methodological details for metagenomic sequencing
654 and downstream analyses, including metagenomic assembly and annotation, reconstruction of
655 metagenome-assembled genomes (MAGs), and gut–brain module (GBM) analysis, are described
656 in Supplementary Material 1. Metagenomic sequencing data have been deposited in the NCBI
657 Sequence Read Archive (BioProject accession number PRJNA1345245).
658
659 **Single-nucleus RNA sequencing**
660 ***Frozen Tissue Nuclear Dissociation***
661 Single-nucleus RNA sequencing (snRNA-seq) was performed by Shanghai Majorbio Bio-Pharm
662 Technology Co., Ltd. (Shanghai, China). Frozen prefrontal cortex (PFC) tissues were
663 homogenized using a glass Dounce tissue grinder (Sigma, USA) with 25 strokes of pestle A and
664 25 strokes of pestle B in 2 mL of ice-cold Nuclei EZ lysis buffer. The homogenate was incubated
665 on ice for 5 minutes, followed by addition of 3 mL of cold lysis buffer and an additional 5-minute
666 incubation. Nuclei were centrifuged at 500 × g for 5 minutes at 4ºC, washed with 5 mL of ice-cold
667 lysis buffer, and incubated on ice for an additional 5 minutes. The nuclear pellet was resuspended
668 and washed in 5 mL of nuclei suspension buffer (NSB; PBS supplemented with 0.01% BSA and
669 0.1% RNase inhibitor, Clontech, USA). Nuclei were resuspended in 2 mL of NSB, filtered through
670 a 35-µm cell strainer (Corning-Falcon, USA), and counted. Nuclei were loaded onto the 10x
671 Genomics Chromium Controller at a final concentration of 1,000 nuclei per µL.
672 ***10x library preparation and sequencing***
673 Gel beads containing unique molecular identifiers (UMIs) and cell barcodes were loaded to near
674 saturation such that each nucleus was paired with one bead in a Gel Bead-in-Emulsion (GEM).
675 After lysis, polyadenylated RNA molecules hybridized to bead-bound oligonucleotides. Beads
676 were collected for reverse transcription, during which each cDNA molecule was tagged at its 3'
677 end (corresponding to the 5' end of the mRNA) with a UMI and cell barcode. Subsequent steps
678 included second-strand synthesis, adaptor ligation, and universal amplification. Sequencing
679 libraries were prepared from randomly fragmented cDNA to enrich 3' transcript ends linked to
680 barcodes and UMIs.
681 All procedures followed the Chromium Single Cell 3' GEM, Library & Gel Bead Kit (v3.1
682 chemistry) manufacturer's protocol. Libraries were quantified using a High Sensitivity DNA Chip

683 (Agilent) on a Bioanalyzer 2100 and a Qubit High Sensitivity DNA Assay (Thermo Fisher
684 Scientific), and sequenced on an Illumina NovaSeq X Plus using paired-end 150-bp chemistry.
685 Detailed methods for snRNA-seq data processing, differential expression, and functional
686 enrichment analyses are provided in Supplementary Material 1. Results of snRNA-seq have been
687 deposited in the NCBI Sequence Read Archive (BioProject accession number PRJNA1345209).
688
689 **Targeted Metabolomics of Fatty Acids and Neurotransmitters in Serum and Brain**
690 ***Targeted metabolomics for fatty acids in brain***
691 Mice were anesthetized with isoflurane, after which venous blood was collected by
692 ophthalmectomy. Brain tissues were harvested, immediately frozen in liquid nitrogen, and stored
693 at −80°C until analysis. Serum was prepared by sequential centrifugation and stored at −80°C until
694 use. Targeted metabolomics analyses were performed by Shanghai BioTree Biomedical
695 Technology Co., Ltd. Brain lipid extraction, sample preparation, and GC–MS–based fatty acid
696 quantification were conducted using standardized protocols. Detailed procedures, including tissue
697 processing, solvent extraction, instrument parameters, and data acquisition settings, are provided
698 in Supplementary Material 1.
699 ***Targeted metabolomics for neurotransmitters in serum and brain***
700 Targeted metabolomics of neurotransmitters in serum and brain was performed using UHPLC–
701 MS/MS following established extraction, derivatization, and analytical procedures. Detailed
702 sample preparation protocols, chromatographic conditions, mass spectrometry parameters, and
703 data processing workflows are provided in Supplementary Material 1.
704
705 **Quantification and statistical analysis**
706 All behavioral and histological analyses were performed under blinded conditions. Statistical
707 analyses were carried out using GraphPad Prism (GraphPad Software, version 10.6.1). Normality
708 was assessed using the Shapiro–Wilk, D'Agostino–Pearson, Anderson–Darling, and
709 Kolmogorov–Smirnov tests. Data are presented as mean ± SEM unless otherwise stated. Normally
710 distributed data were compared using two-tailed (or one-tailed, as specified in figure legends)
711 unpaired Student's *t*-tests. Non-normally distributed data were analyzed using two-tailed (or one-
712 tailed, as specified) Mann–Whitney U tests. P values < 0.05 were considered statistically
713 significant. Exact sample sizes (n) and statistical tests used are reported in the figure legends, and
714 precise P values are indicated in the figures. All raw data used in this study are provided in
715 Supplementary Tables S1 and S2.
716
717 **Supplemental information**
718 **Supplementary Material 1.**
719 Supplementary Methods and Figs. S1–S7 related to Figs. 1–6.
720 **Supplementary Material 2.**
721 Table S1. Raw data related to Figs. 1–6.
722 **Supplementary Material 3.**

Table S2. Raw data related to Figs. S1–S7.

Supplementary Material 4.

Video S1. Voluntary intake of PS128-containing or blank jelly by mice.

Supplementary Material 5.

Video S2. Behavioral statistics from the olfactory habituation/dishabituation test, related to Fig. S1.

Supplementary Material 6.

Video S3. Four specific behaviors in the olfactory habituation/dishabituation test, related to Fig. S1.

Acknowledgements

We thank the ECNU Multifunctional Platform for Innovation (101) for their mouse breeding service.

Authors' contributions

YHP and XBY conceived and supervised the project and obtained funding. YMC, YXC, and SZ conducted behavioral, histological, and molecular analyses. JLC, YXC, YMC, TAL, and SSG conducted data processing. YMC, YXC, and YHP conducted data analysis and figure organization. YHP, XBY, YCT, YWL, JM, WZ, and HPL contributed to the discussion and data interpretation. YMC, YXC, YHP, and XBY wrote the manuscript. All authors read and approved the final manuscript.

Funding

This work was supported by the National Natural Science Foundation of China (grant numbers 31100273 to YHP and 81941013 and 32271022 to XBY); the Key Laboratory of Brain Functional Genomics at East China Normal University (grant number 23SKBFGK2 to YHP and HL); the National Key Research and Development Program of China (grant number 2022YFC2705200); the National Natural Science Foundation of China–Israel Science Foundation Cooperative Research Project (grant number 32061143016); and the Fundamental Research Funds for the Central Universities.

Data availability

Whole-genome sequencing data for *Lactiplantibacillus plantarum* PS128 have been deposited in NCBI-SRA under accession number PRJNA1345344. 16S rRNA sequencing data have been deposited in NCBI-SRA under accession number PRJNA1345244. Metagenomic sequencing data have been deposited in NCBI-SRA under accession number PRJNA1345245. Single-nucleus RNA sequencing data have been deposited in NCBI-SRA under accession number PRJNA1345209.

Declarations

Ethics approval and consent to participate

All animal procedures were approved by the Institutional Animal Care and Use Committee of East China Normal University (approval no. m20241106) and were conducted in accordance with institutional guidelines.

Consent for publication

Not applicable.

Competing interests

The authors declare that they have no competing interests.

Author details

[1]Key Laboratory of Brain Functional Genomics of Shanghai and Ministry of Education, Institute of Brain Functional Genomics, School of Life Science and the Collaborative Innovation Center for Brain Science, East China Normal University, Shanghai 200062, China. [2]Institute of Biochemistry and Molecular Biology, National Yang Ming Chiao Tung University, Taipei 11221, Taiwan. [3]Institute of Mechanobiology and Medical Engineering, School of Life Sciences and Biotechnology, Shanghai Jiao Tong University, Shanghai 201100, China. [4]Shanghai Institute of Nutrition and Health, University of Chinese Academy of Sciences, Chinese Academy of Sciences, Shanghai 200031, China.

Reference

1. Cao XX, Jia JY, Li Z, Guo SM, Duan JL, Ma J et al. *Cadherin 11* regulates presynaptic vesicle trafficking and neuronal activity in autism-related brain circuit. Mol Psychiatr. 2025; doi:10.1038/s41380-025-03141-7.
2. Shaw KA, Bilder DA, McArthur D, Williams AR, Amoakohene E, Bakian AV et al. Early Identification of Autism Spectrum Disorder Among Children Aged 4 Years - Autism and Developmental Disabilities Monitoring Network, 11 Sites, United States, 2020. MMWR Surveill Summ. 2023; doi:10.15585/mmwr.ss7201a1.
3. Collaborators GBoDSAS. The global epidemiology and health burden of the autism spectrum: findings from the Global Burden of Disease Study 2021. Lancet Psychiatry. 2025; doi:10.1016/s2215-0366(24)00363-8.
4. Pan YH, Wu N, Yuan XB. Toward a Better Understanding of Neuronal Migration Deficits in Autism Spectrum Disorders. Front Cell Dev Biol. 2019; doi:10.3389/fcell.2019.00205.
5. Tarlungeanu DC, Deliu E, Dotter CP, Kara M, Janiesch PC, Scalise M et al. Impaired Amino Acid Transport at the Blood Brain Barrier Is a Cause of Autism Spectrum Disorder. Cell. 2016; doi:10.1016/j.cell.2016.11.013.
6. Liu A, Zhou W, Qu L, He F, Wang H, Wang Y et al. Altered Urinary Amino Acids in Children With Autism Spectrum Disorders. Front Cell Neurosci. 2019; doi:10.3389/fncel.2019.00007.
7. Wang L, Zheng R, Xu Y, Zhou Z, Guan P, Wu Y et al. Altered Metabolic Characteristics in Plasma of Young Boys with Autism Spectrum Disorder. J Autism Dev Disord. 2022; doi:10.1007/s10803-021-05364-3.
8. Wang M, Liang Z, Zhuang H, Cao X, Ma G, Sun Y et al. *Cntn4* Gene Deficiency Promotes Autism-Like Phenotypes Associated with Gut Microbiota Perturbations and Gut-Brain Axis Metabolomic Alterations in Mice. Mol Neurobiol. 2025; doi:10.1007/s12035-025-05567-0.
9. Wang P, Wu P-F, Wang H-J, Liao F, Wang F, Chen J-G. Gut microbiome-derived ammonia modulates stress vulnerability in the host. Nat Metab. 2023; doi:10.1038/s42255-023-00909-5.
10. Needham BD, Funabashi M, Adame MD, Wang Z, Boktor JC, Haney J et al. A gut-derived metabolite alters brain activity and anxiety behaviour in mice. Nature. 2022; doi:10.1038/s41586-022-04396-8.
11. Holbert CE, Cullen MT, Casero RA, Stewart TM. Polyamines in cancer: integrating organismal metabolism and antitumour immunity. Nat Rev Cancer. 2022; doi:10.1038/s41568-022-00473-2.

12. Vrijsen S, Houdou M, Cascalho A, Eggermont J, Vangheluwe P. Polyamines in Parkinson's Disease: Balancing Between Neurotoxicity and Neuroprotection. Annu Rev Biochem. 2023; doi:10.1146/annurev-biochem-071322-021330.
13. Siani-Rose M, Cox S, Goldstein B, Abrams D, Taylor M, Kurek I. Cannabis-Responsive Biomarkers: A Pharmacometabolomics-Based Application to Evaluate the Impact of Medical Cannabis Treatment on Children with Autism Spectrum Disorder. Cannabis Cannabinoid Res. 2023; doi:10.1089/can.2021.0129.
14. Snigdha S, Ha K, Tsai P, Dinan TG, Bartos JD, Shahid M. Probiotics: Potential novel therapeutics for microbiota-gut-brain axis dysfunction across gender and lifespan. Pharmacol Ther. 2022; doi:10.1016/j.pharmthera.2021.107978.
15. Liu YW, Liong MT, Chung YE, Huang HY, Peng WS, Cheng YF et al. Effects of *Lactobacillus plantarum* PS128 on Children with Autism Spectrum Disorder in Taiwan: A Randomized, Double-Blind, Placebo-Controlled Trial. Nutrients. 2019; doi:10.3390/nu11040820.
16. Mensi MM, Rogantini C, Marchesi M, Borgatti R, Chiappedi M. *Lactobacillus plantarum* PS128 and Other Probiotics in Children and Adolescents with Autism Spectrum Disorder: A Real-World Experience. Nutrients. 2021; doi:10.3390/nu13062036.
17. Gantois I, Khoutorsky A, Popic J, Aguilar-Valles A, Freemantle E, Cao R et al. Metformin ameliorates core deficits in a mouse model of fragile X syndrome. Nat Med. 2017; doi:10.1038/nm.4335.
18. Protic DD, Aishworiya R, Salcedo-Arellano MJ, Tang SJ, Milisavljevic J, Mitrovic F et al. Fragile X Syndrome: From Molecular Aspect to Clinical Treatment. Int J Mol Sci. 2022; doi:10.3390/ijms23041935.
19. Guo PF, Yang XY, Guo XM, Yang HE, Pan J, Li Y. Dietary fish oil improves autistic behaviors and gut homeostasis by altering the gut microbial composition in a mouse model of fragile X syndrome. Brain Behav Immun. 2023; doi:10.1016/j.bbi.2023.02.019.
20. Goo N, Bae HJ, Park K, Kim J, Jeong Y, Cai M et al. The effect of fecal microbiota transplantation on autistic-like behaviors in *Fmr1* KO mice. Life Sci. 2020; doi:10.1016/j.lfs.2020.118497.
21. Cupolillo D, Hoxha E, Faralli A, De Luca A, Rossi F, Tempia F et al. Autistic-Like Traits and Cerebellar Dysfunction in Purkinje Cell *PTEN* Knock-Out Mice. Neuropsychopharmacology. 2016; doi:10.1038/npp.2015.339.
22. Holmberg SM, Feeney RH, Prasoodanan PKV, Puértolas-Balint F, Singh DK, Wongkuna S et al. The gut commensal *Blautia* maintains colonic mucus function under low-fiber consumption through secretion of short-chain fatty acids. Nat Commun. 2024; doi:10.1038/s41467-024-47594-w.
23. Gong J, Chen F, Jiang B, Zhou B, Ma X, Wang M et al. Associations between blood systemic inflammatory markers and anxiety in *Helicobacter pylori*-infected patients. Front Psychiatry. 2025; doi:10.3389/fpsyt.2025.1671858.
24. Hsu TW, Chu CS, Tsai SJ, Bai YM, Su TP, Chen TJ et al. Risk of Major Mental Disorder after Severe Bacterial Infections in Children and Adolescents: A Nationwide Longitudinal Study. Neuropsychobiology. 2022; doi:10.1159/000526984.
25. Valles-Colomer M, Falony G, Darzi Y, Tigchelaar EF, Wang J, Tito RY et al. The neuroactive potential of the human gut microbiota in quality of life and depression. Nat Microbiol. 2019; doi:10.1038/s41564-018-0337-x.
26. Agirman G, Hsiao EY. SnapShot: The microbiota-gut-brain axis. Cell. 2021; doi:10.1016/j.cell.2021.03.022.
27. Needham BD, Adame MD, Serena G, Rose DR, Preston GM, Conrad MC et al. Plasma and Fecal Metabolite Profiles in Autism Spectrum Disorder. Biol Psychiatry. 2021; doi:10.1016/j.biopsych.2020.09.025.
28. Hsiao EY, McBride SW, Hsien S, Sharon G, Hyde ER, McCue T et al. Microbiota modulate behavioral and physiological abnormalities associated with neurodevelopmental disorders. Cell. 2013; doi:10.1016/j.cell.2013.11.024.
29. Sharon G, Cruz NJ, Kang DW, Gandal MJ, Wang B, Kim YM et al. Human Gut Microbiota from Autism Spectrum Disorder Promote Behavioral Symptoms in Mice. Cell. 2019; doi:10.1016/j.cell.2019.05.004.
30. Chen CM, Wu CC, Huang CL, Chang MY, Cheng SH, Lin CT et al. *Lactobacillus plantarum* PS128 Promotes Intestinal Motility, Mucin Production, and Serotonin Signaling in Mice. Probiotics Antimicrob Proteins. 2022; doi:10.1007/s12602-021-09814-3.
31. Cheng J, Tong J, Li C, Wang Z, Li H, Ren M et al. Probiotic Characterization of *Lactiplantibacillus paraplantarum* SDN1.2 and Its Anti-Inflammatory Effect on *Klebsiella pneumoniae*-Infected Mammary Glands. Vet Sci. 2025; doi:10.3390/vetsci12040323.
32. Mihailović M, Soković Bajić S, Arambašić Jovanović J, Brdarić E, Dinić S, Grdović N et al. Beneficial Effects of Probiotic *Lactobacillus paraplantarum* BGCG11 on Pancreatic and Duodenum Function in Diabetic Rats. Int J Mol Sci. 2024; doi:10.3390/ijms25147697.

33. Kong XJ, Liu J, Liu K, Koh M, Sherman H, Liu S et al. Probiotic and Oxytocin Combination Therapy in Patients with Autism Spectrum Disorder: A Randomized, Double-Blinded, Placebo-Controlled Pilot Trial. Nutrients. 2021; doi:10.3390/nu13051552.
34. Zhang C, Zhen Y, Weng Y, Lin J, Xu X, Ma J et al. Research progress on the microbial metabolism and transport of polyamines and their roles in animal gut homeostasis. J Anim Sci Biotechnol. 2025; doi:10.1186/s40104-025-01193-x.
35. Houdou M, Jacobs N, Coene J, Azfar M, Vanhoutte R, Van den Haute C et al. Novel Green Fluorescent Polyamines to Analyze ATP13A2 and ATP13A3 Activity in the Mammalian Polyamine Transport System. Biomolecules. 2023; doi:10.3390/biom13020337.
36. Balint B, Damasio J, Magrinelli F, Guerreiro R, Bras J, Bhatia KP. Psychiatric Manifestations of *ATP13A2* Mutations. Mov Disord Clin Pract. 2020; doi:10.1002/mdc3.13034.
37. Lesca G, Rudolf G, Labalme A, Hirsch E, Arzimanoglou A, Genton P et al. Epileptic encephalopathies of the Landau-Kleffner and continuous spike and waves during slow-wave sleep types: genomic dissection makes the link with autism. Epilepsia. 2012; doi:10.1111/j.1528-1167.2012.03559.x.
38. Biamino E, Di Gregorio E, Belligni EF, Keller R, Riberi E, Gandione M et al. A novel 3q29 deletion associated with autism, intellectual disability, psychiatric disorders, and obesity. Am J Med Genet B Neuropsychiatr Genet. 2016; doi:10.1002/ajmg.b.32406.
39. Vallipuram J, Grenville J, Crawford DA. The E646D-ATP13A4 mutation associated with autism reveals a defect in calcium regulation. Cell Mol Neurobiol. 2010; doi:10.1007/s10571-009-9445-8.
40. van Veen S, Irala D, Sakers K, Savage J, Séjourné G, Bindu DS et al. Astrocytic polyamine transport by ATP13A4 tunes excitatory synaptic transmission. medRxiv. 2025; doi:10.1101/2025.04.04.25325117.
41. Koh W, Kwak H, Cheong E, Lee CJ. GABA tone regulation and its cognitive functions in the brain. Nat Rev Neurosci. 2023; doi:10.1038/s41583-023-00724-7.
42. De Sales-Millán A, Reyes-Ferreira P, Aguirre-Garrido JF, Corral-Guillé I, Barrientos-Ríos R, Velázquez-Aragón JA. Comprehensive Analysis of Gut Microbiota Composition and Functional Metabolism in Children with Autism Spectrum Disorder and Neurotypical Children: Implications for Sex-Based Differences and Metabolic Dysregulation. Int J Mol Sci. 2024; doi:10.3390/ijms25126701.
43. Golbaghi N, Naeimi S, Darvishi A, Najari N, Cussotto S. Probiotics in autism spectrum disorder: Recent insights from animal models. Autism. 2024; doi:10.1177/13623613241246911.
44. Takyi E, Nirmalkar K, Adams J, Krajmalnik-Brown R. Interventions targeting the gut microbiota and their possible effect on gastrointestinal and neurobehavioral symptoms in autism spectrum disorder. Gut Microbes. 2025; doi:10.1080/19490976.2025.2499580.
45. Sgritta M, Dooling SW, Buffington SA, Momin EN, Francis MB, Britton RA et al. Mechanisms Underlying Microbial-Mediated Changes in Social Behavior in Mouse Models of Autism Spectrum Disorder. Neuron. 2019; doi:10.1016/j.neuron.2018.11.018.
46. Yu Y, Zhang B, Ji P, Zuo Z, Huang Y, Wang N et al. Changes to gut amino acid transporters and microbiome associated with increased E/I ratio in *Chd8*$^{+/-}$ mouse model of ASD-like behavior. Nat Commun. 2022; doi:10.1038/s41467-022-28746-2.
47. Chen CM, Wu CC, Kim Y, Hsu WY, Tsai YC, Chiu SL. Enhancing social behavior in an autism spectrum disorder mouse model: investigating the underlying mechanisms of *Lactiplantibacillus plantarum* intervention. Gut Microbes. 2024; doi:10.1080/19490976.2024.2359501.
48. Huang W, Liao C-C, Han Y, Lv J, Lei M, Li Y et al. Co-activation of Akt, Nrf2, and NF-κB signals under UPRER in torpid *Myotis ricketti* bats for survival. Commun Biol. 2020; doi:10.1038/s42003-020-01378-2.
49. Corcoran BM, Stanton C, Fitzgerald GF, Ross RP. Survival of probiotic lactobacilli in acidic environments is enhanced in the presence of metabolizable sugars. Appl Environ Microbiol. 2005; doi:10.1128/aem.71.6.3060-3067.2005.
50. Azat R, Liu Y, Li W, Kayir A, Lin DB, Zhou WW et al. Probiotic properties of lactic acid bacteria isolated from traditionally fermented Xinjiang cheese. J Zhejiang Univ-SCI B. 2016; doi:10.1631/jzus.B1500250.
51. Schwieger F, Tebbe CC. A new approach to utilize PCR-single-strand-conformation polymorphism for 16s rRNA gene-based microbial community analysis. Appl Environ Microbiol. 1998; doi:10.1128/AEM.64.12.4870-4876.1998.

Figure titles and legends

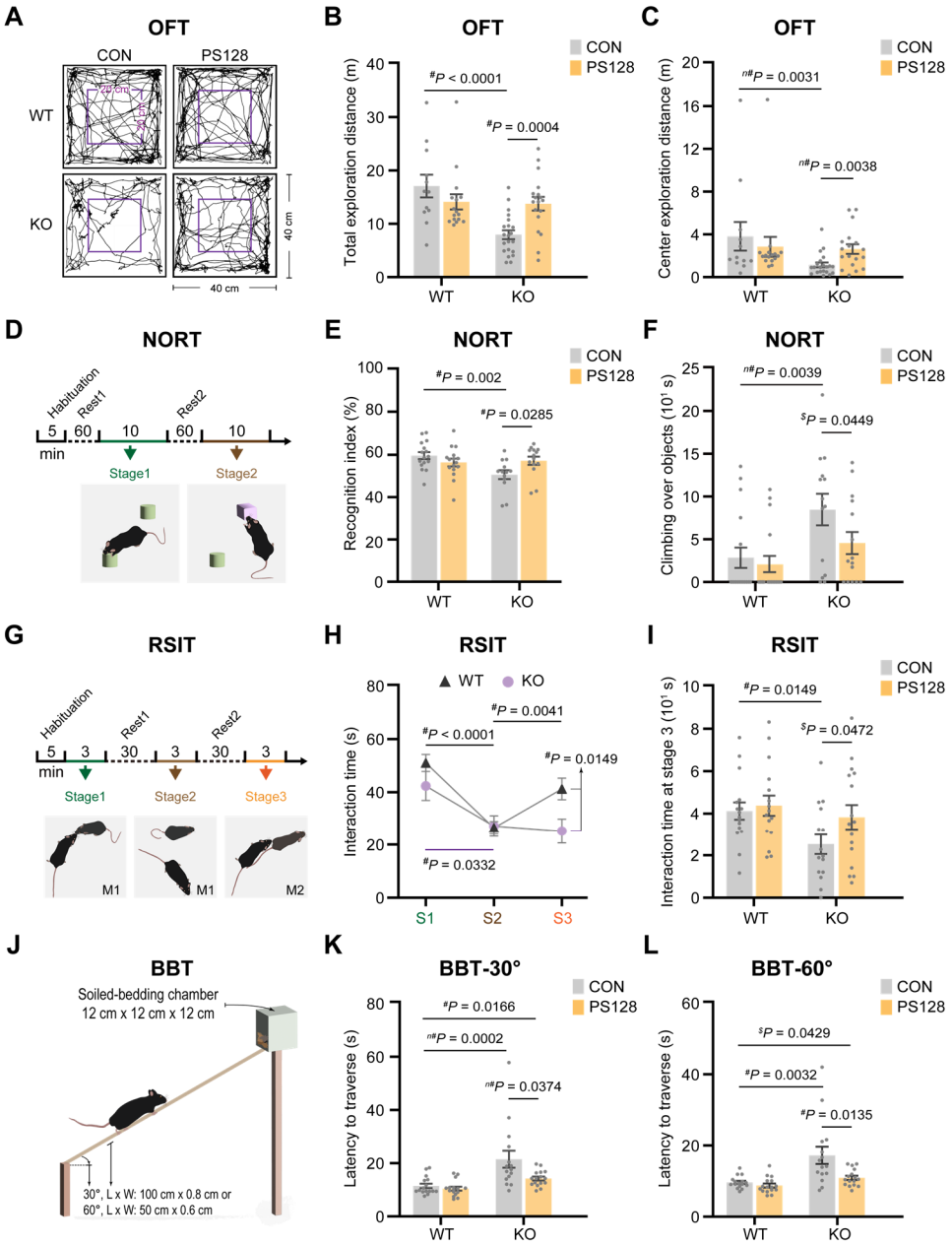

Fig. 1 Microbiota-targeted intervention alleviates autism-like behaviors in *Fmr1* KO mice. A–C Representative traces in the open-field test (OFT) (**A**), total exploration distance (**B**), and center exploration distance (**C**), n = 12–21. **D–F** Schematic of the novel object recognition test (NORT) (**D**), recognition index (%) = (novel) / (novel + familiar) x 100, based on sniffing time (**E**), and total time spent climbing over objects (**F**), n = 13–18. **G–I** Schematic of the reciprocal social interaction test (RSIT) (**G**), interaction time with familiar or novel mice across three stages (**H**), and interaction time at Stage 3 (**I**), n = 15–16. S, stage. **J–L** Schematic of the balance beam test (BBT) (**J**), latency to traverse a 30° beam (**K**), or a 60° beam (**L**), n = 15–16. Data are presented as mean ± S.E.M. and gray dots indicate individual mice. One-tailed ($^{\$}$) or two-tailed ($^{\#}$) Student's t-test and two-tailed ($^{n\#}$) Mann–Whitney U test were used where appropriate. A P value < 0.05 was considered statistically significant. See also Fig. S1.

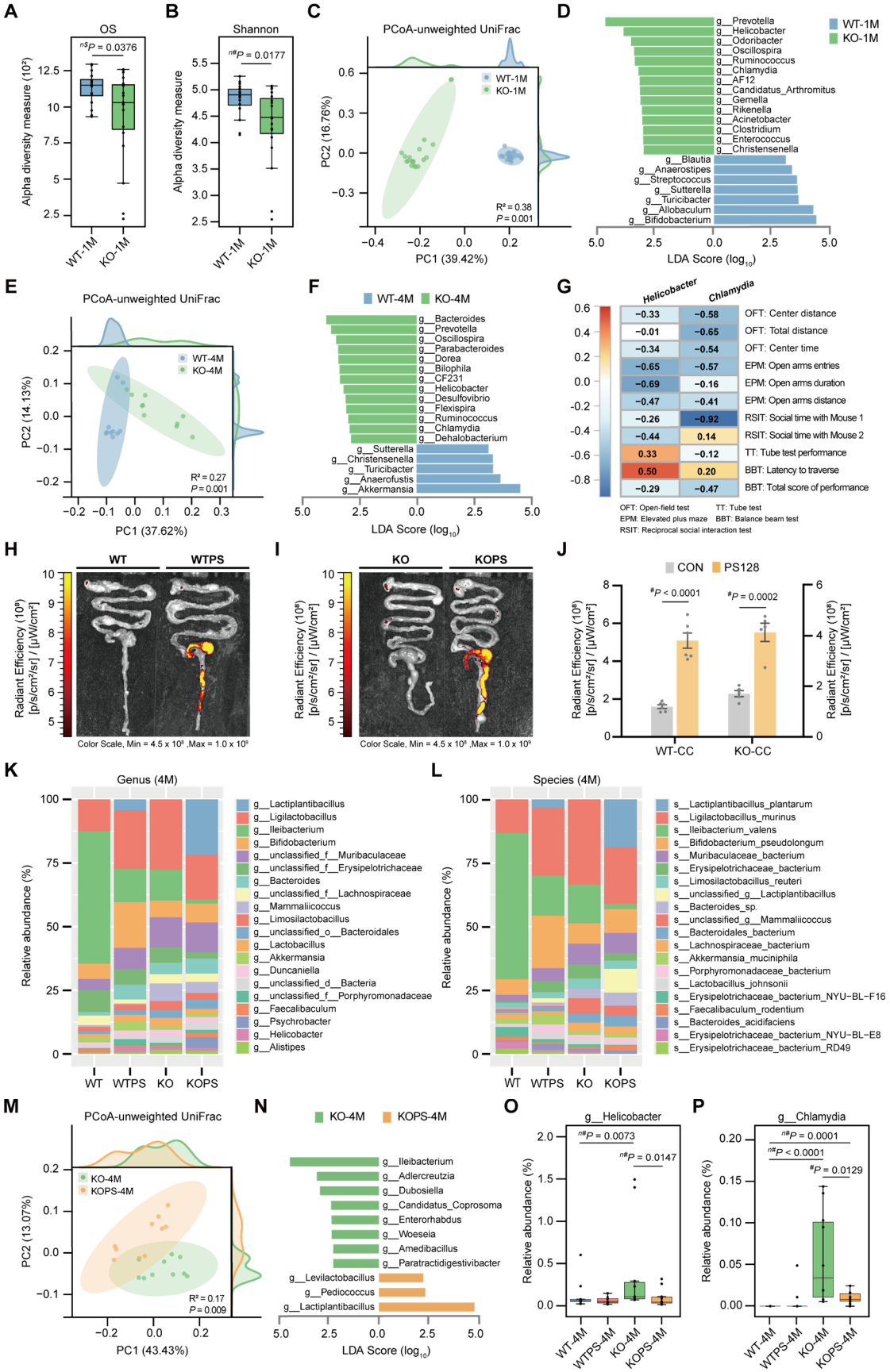
A
OS
n$P = 0.0376
Alpha diversity measure (10²)
WT-1M
KO-1M
B
Shannon
n#P = 0.0177
Alpha diversity measure
C
PCoA-unweighted UniFrac
WT-1M
KO-1M
PC2 (16.76%)
PC1 (39.42%)
R² = 0.38
P = 0.001
D
WT-1M
KO-1M
g__Prevotella
g__Helicobacter
g__Odoribacter
g__Oscillospira
g__Ruminococcus
g__Chlamydia
g__AF12
g__Candidatus_Arthromitus
g__Gemella
g__Rikenella
g__Acinetobacter
g__Clostridium
g__Enterococcus
g__Christensenella
g__Blautia
g__Anaerostipes
g__Streptococcus
g__Sutterella
g__Turicibacter
g__Allobaculum
g__Bifidobacterium
LDA Score (log10)
E
PCoA-unweighted UniFrac
WT-4M
KO-4M
PC2 (14.13%)
PC1 (37.62%)
R² = 0.27
P = 0.001
F
WT-4M
KO-4M
g__Bacteroides
g__Prevotella
g__Oscillospira
g__Parabacteroides
g__Dorea
g__Bilophila
g__CF231
g__Helicobacter
g__Desulfovibrio
g__Flexispira
g__Ruminococcus
g__Chlamydia
g__Dehalobacterium
g__Sutterella
g__Christensenella
g__Turicibacter
g__Anaerofustis
g__Akkermansia
LDA Score (log10)
G
Helicobacter
Chlamydia
OFT: Center distance −0.33 −0.58
OFT: Total distance −0.01 −0.65
OFT: Center time −0.34 −0.54
EPM: Open arms entries −0.65 −0.57
EPM: Open arms duration −0.69 −0.16
EPM: Open arms distance −0.47 −0.41
RSIT: Social time with Mouse 1 −0.26 −0.92
RSIT: Social time with Mouse 2 −0.44 0.14
TT: Tube test performance 0.33 −0.12
BBT: Latency to traverse 0.50 0.20
BBT: Total score of performance −0.29 −0.47
OFT: Open-field test
TT: Tube test
EPM: Elevated plus maze
BBT: Balance beam test
RSIT: Reciprocal social interaction test
H
WT
WTPS
Radiant Efficiency (10⁸) [p/s/cm²/sr] / [μW/cm²]
Color Scale, Min = 4.5 x 10⁸ ,Max = 1.0 x 10⁹
I
KO
KOPS
Radiant Efficiency (10⁸) [p/s/cm²/sr] / [μW/cm²]
Color Scale, Min = 4.5 x 10⁸ ,Max = 1.0 x 10⁹
J
CON
PS128
#P < 0.0001
#P = 0.0002
Radiant Efficiency (10⁸) [p/s/cm²/sr] / [μW/cm²]
WT-CC
KO-CC
K
Genus (4M)
Relative abundance (%)
g__Lactiplantibacillus
g__Ligilactobacillus
g__Ileibacterium
g__Bifidobacterium
g__unclassified_f__Muribaculaceae
g__unclassified_f__Erysipelotrichaceae
g__Bacteroides
g__unclassified_f__Lachnospiraceae
g__Mammaliicoccus
g__Limosilactobacillus
g__unclassified_o__Bacteroidales
g__Lactobacillus
g__Akkermansia
g__Duncaniella
g__unclassified_d__Bacteria
g__unclassified_f__Porphyromonadaceae
g__Faecalibaculum
g__Psychrobacter
g__Helicobacter
g__Alistipes
WT
WTPS
KO
KOPS
L
Species (4M)
Relative abundance (%)
s__Lactiplantibacillus_plantarum
s__Ligilactobacillus_murinus
s__Ileibacterium_valens
s__Bifidobacterium_pseudolongum
s__Muribaculaceae_bacterium
s__Erysipelotrichaceae_bacterium
s__Limosilactobacillus_reuteri
s__unclassified_g__Lactiplantibacillus
s__Bacteroides_sp.
s__unclassified_g__Mammaliicoccus
s__Bacteroidales_bacterium
s__Lachnospiraceae_bacterium
s__Akkermansia_muciniphila
s__Porphyromonadaceae_bacterium
s__Lactobacillus_johnsonii
s__Erysipelotrichaceae_bacterium_NYU−BL−F16
s__Faecalibaculum_rodentium
s__Bacteroides_acidifaciens
s__Erysipelotrichaceae_bacterium_NYU−BL−E8
s__Erysipelotrichaceae_bacterium_RD49
WT
WTPS
KO
KOPS
M
PCoA-unweighted UniFrac
KO-4M
KOPS-4M
PC2 (13.07%)
PC1 (43.43%)
R² = 0.17
P = 0.009
N
KO-4M
KOPS-4M
g__Ileibacterium
g__Adlercreutzia
g__Dubosiella
g__Candidatus_Coprosoma
g__Enterorhabdus
g__Woeseia
g__Amedibacillus
g__Paratractidigestivibacter
g__Levilactobacillus
g__Pediococcus
g__Lactiplantibacillus
LDA Score (log10)
O
g__Helicobacter
n#P = 0.0073
n#P = 0.0147
Relative abundance (%)
WT-4M
WTPS-4M
KO-4M
KOPS-4M
P
g__Chlamydia
n#P = 0.0001
n#P < 0.0001
#P = 0.0129
Relative abundance (%)
WT-4M
WTPS-4M
KO-4M
KOPS-4M

926

927 **Fig. 2 Microbiota-targeted intervention reshapes gut microbial community structure in *Fmr1* KO mice. A–D**
928 Gut microbiota analysis of 1-month-old *Fmr1* KO mice and their wild-type (WT) littermates without PS128
929 intervention. Observed species (**A**). Shannon diversity index (**B**). Principal coordinates analysis (PCoA) plot based on
930 unweighted UniFrac distances (**C**). Histogram of linear discriminant analysis (LDA) scores from LEfSe analysis at
931 the genus level, logarithmic LDA score cutoff > 3.0, $P < 0.05$ (**D**), $n = 19–20$. **E** and **F** Gut microbiota analysis of 4-
932 month-old *Fmr1* KO mice and their WT littermates following 3 months of PS128 supplementation. PCoA plot (**E**).
933 Histogram of logarithmic LDA scores, cutoff > 2.5, $P < 0.05$ (**F**), $n = 10$. **G** Spearman's rank correlation analysis
934 between the relative abundance of *Helicobacter* and *Chlamydia* and behavioral performance in 4-month-old *Fmr1* KO
935 mice, $n = 10–11$.**H–J** Biodistribution of PS128 in the gastrointestinal tract. Representative ex vivo fluorescence images
936 of the gut from *Fmr1* KO mice and their WT littermates after oral gavage with fluorescently labeled PS128 (**H** and **I**).
937 Average radiant efficiency quantified from the cecum and colon (CC) (**J**), $n = 5–6$. **K** and **L** Relative abundance of
938 gut microbiota at the genus (**K**) and species (**L**) levels in 4-month-old groups, $n = 11–13$. **M** and **N** Gut microbiota
939 analysis comparing 4-month-old *Fmr1* KO mice with or without PS128 treatment (KO or KOPS). PCoA plot (**M**).
940 Histogram of logarithmic LDA scores, cutoff > 2.2, $P < 0.05$ (**N**), $n = 10-11$. **O** and **P** Relative abundance of
941 *Helicobacter* (**O**) and *Chlamydia* (**P**) across 4-month-old groups, $n = 10$. Data are presented as mean ± S.E.M. and
942 each dot represents an individual mouse. Statistical significance was determined by two-tailed Student's *t*-test ($^{\#}$), one-
943 tailed ($^{n\$}$), or two-tailed ($^{n\#}$) Mann–Whitney U test, as appropriate. A P value < 0.05 was considered significant. See
944 also Figs. S2 and S3.

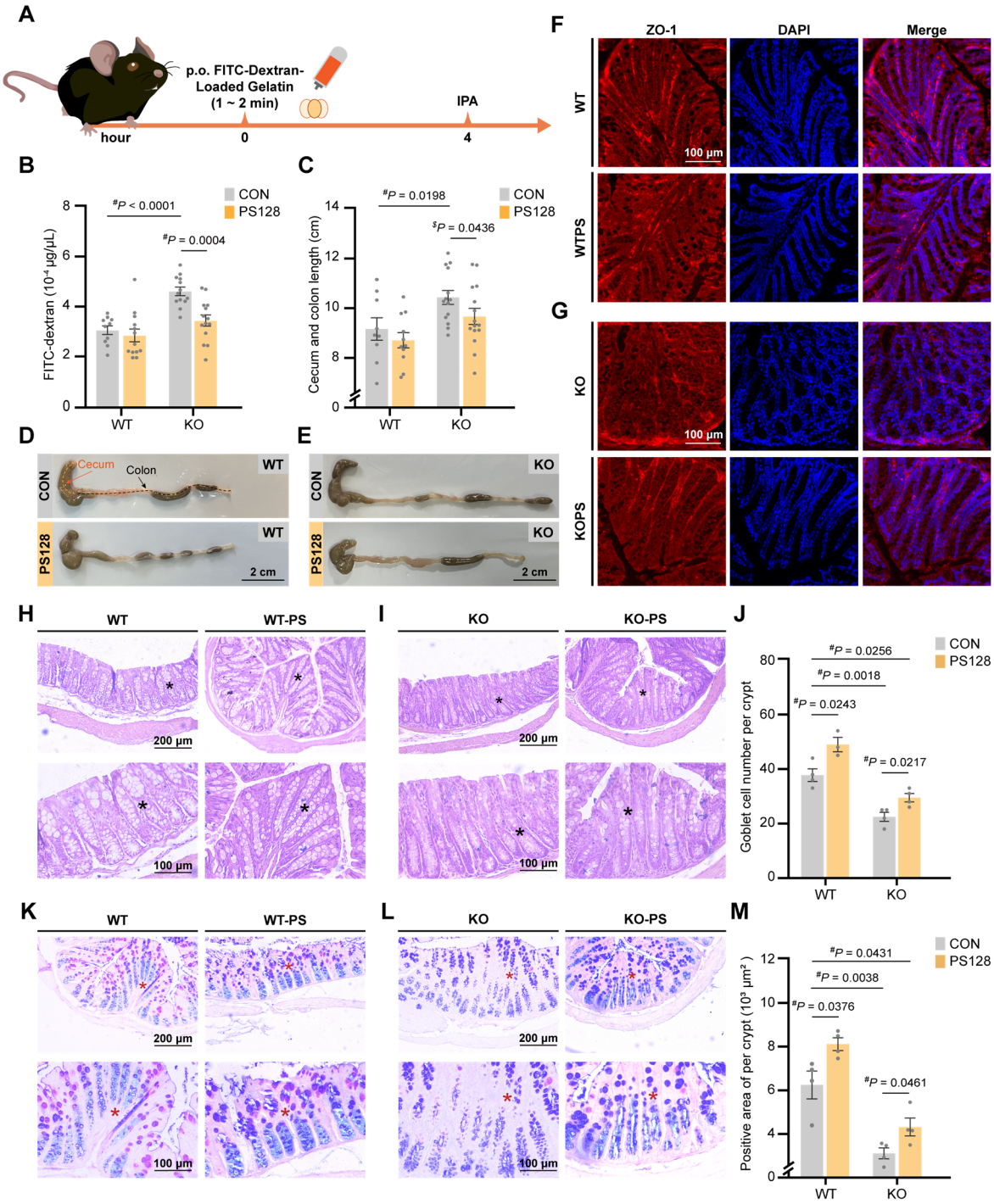

Fig. 3 Microbiota remodeling restores intestinal barrier integrity in *Fmr1* KO mice. A and **B** Assessment of intestinal permeability. Schematic of intestinal permeability assay (IPA) (**A**). Serum FITC-dextran concentrations after orally self-consumed FITC–dextran–loaded gelatin (**B**), n = 10–14. **C–E** Gross anatomical assessment of the large intestine. Average length of the cecum and colon, n = 9–15 (**C**). Representative images of dissected tissues (**D** and **E**). **F** and **G** Colon integrity. Representative immunofluorescence images of colonic sections stained for ZO-1 (red) and nuclei (DAPI, blue). Scale bar, 100 μm. **H–J** Histological evaluation of colonic architecture. Representative H&E–stained sections of *Fmr1* KO and their WT littermates with/without PS128 intervention (**H** and **I**).

953 Quantification of goblet cells per crypt (average of 3 crypts per section, 3 sections per mouse), $n = 3–4$ (**J**). Scale bars,
954 200 µm and 100 µm. **K–M** Analysis of mucin production. Representative AB–PAS–stained sections showing acidic
955 and neutral mucins in blue and magenta for KO and their WT littermates with/without PS128 intervention (**K** and **L**).
956 Quantification of MUC2-positive light blue and dark purple areas per crypt, 3 crypts per mouse, $n = 4$ (**M**). Scale bars,
957 200 µm and 100 µm. Data are mean ± S.E.M. and each dot represents an individual mouse. Statistical significance
958 was determined by one-tailed ($^{\$}$) or two-tailed ($^{\#}$) Student's *t*-test. A P value < 0.05 was considered significant.

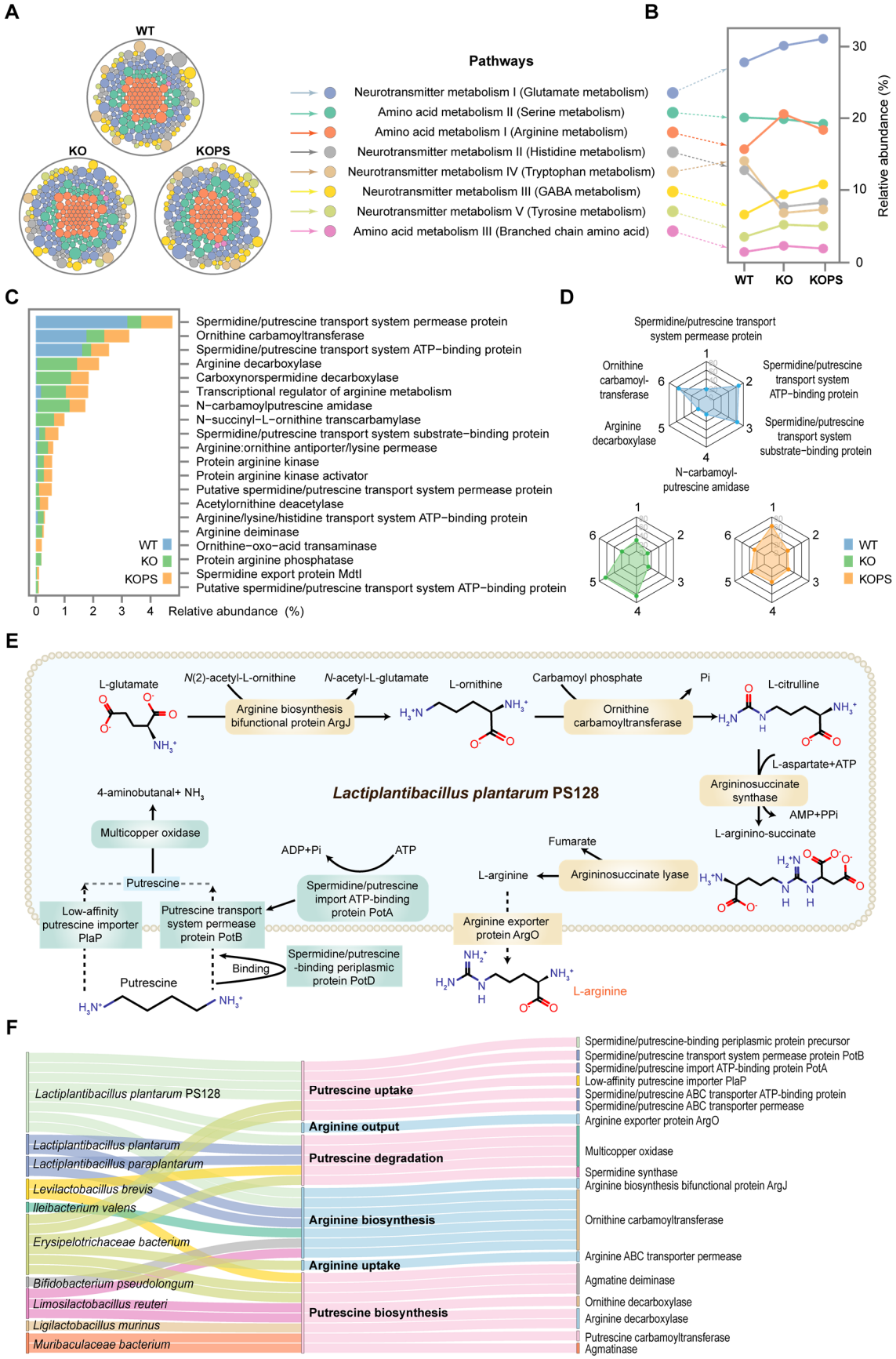
A
WT
KO
KOPS
Pathways
Neurotransmitter metabolism I (Glutamate metabolism)
Amino acid metabolism II (Serine metabolism)
Amino acid metabolism I (Arginine metabolism)
Neurotransmitter metabolism II (Histidine metabolism)
Neurotransmitter metabolism IV (Tryptophan metabolism)
Neurotransmitter metabolism III (GABA metabolism)
Neurotransmitter metabolism V (Tyrosine metabolism)
Amino acid metabolism III (Branched chain amino acid)
B
Relative abundance (%)
WT
KO
KOPS
C
Spermidine/putrescine transport system permease protein
Ornithine carbamoyltransferase
Spermidine/putrescine transport system ATP−binding protein
Arginine decarboxylase
Carboxynorspermidine decarboxylase
Transcriptional regulator of arginine metabolism
N−carbamoylputrescine amidase
N−succinyl−L−ornithine transcarbamylase
Spermidine/putrescine transport system substrate−binding protein
Arginine:ornithine antiporter/lysine permease
Protein arginine kinase
Protein arginine kinase activator
Putative spermidine/putrescine transport system permease protein
Acetylornithine deacetylase
Arginine/lysine/histidine transport system ATP−binding protein
Arginine deiminase
Ornithine−oxo−acid transaminase
Protein arginine phosphatase
Spermidine export protein MdtI
Putative spermidine/putrescine transport system ATP−binding protein
Relative abundance (%)
D
Spermidine/putrescine transport system permease protein
Ornithine carbamoyl-transferase
Spermidine/putrescine transport system ATP−binding protein
Arginine decarboxylase
Spermidine/putrescine transport system substrate−binding protein
N−carbamoyl-putrescine amidase
WT
KO
KOPS
E
L-glutamate
N(2)-acetyl-L-ornithine
Arginine biosynthesis bifunctional protein ArgJ
N-acetyl-L-glutamate
L-ornithine
Carbamoyl phosphate
Ornithine carbamoyltransferase
Pi
L-citrulline
L-aspartate+ATP
Argininosuccinate synthase
AMP+PPi
L-arginino-succinate
Argininosuccinate lyase
Fumarate
L-arginine
Arginine exporter protein ArgO
L-arginine
Lactiplantibacillus plantarum PS128
4-aminobutanal+ NH3
Multicopper oxidase
Putrescine
ADP+Pi
ATP
Spermidine/putrescine import ATP-binding protein PotA
Low-affinity putrescine importer PlaP
Putrescine transport system permease protein PotB
Binding
Spermidine/putrescine -binding periplasmic protein PotD
Putrescine
F
Lactiplantibacillus plantarum PS128
Lactiplantibacillus plantarum
Lactiplantibacillus paraplantarum
Levilactobacillus brevis
Ileibacterium valens
Erysipelotrichaceae bacterium
Bifidobacterium pseudolongum
Limosilactobacillus reuteri
Ligilactobacillus murinus
Muribaculaceae bacterium
Putrescine uptake
Arginine output
Putrescine degradation
Arginine biosynthesis
Arginine uptake
Putrescine biosynthesis
Spermidine/putrescine-binding periplasmic protein precursor
Spermidine/putrescine transport system permease protein PotB
Spermidine/putrescine import ATP-binding protein PotA
Low-affinity putrescine importer PlaP
Spermidine/putrescine ABC transporter ATP-binding protein
Spermidine/putrescine ABC transporter permease
Arginine exporter protein ArgO
Multicopper oxidase
Spermidine synthase
Arginine biosynthesis bifunctional protein ArgJ
Ornithine carbamoyltransferase
Arginine ABC transporter permease
Agmatine deiminase
Ornithine decarboxylase
Arginine decarboxylase
Putrescine carbamoyltransferase
Agmatinase

959

960 **Fig. 4 Microbiota-targeted intervention reprograms the gut arginine–ornithine–polyamine metabolic pathway.**
961 **A–D** Distribution of gut–brain modules (GBMs) at the species level. Each GBM is represented by a distinct color (**A**).
962 GBMs were classified into eight functional clusters based on their association with gut–brain metabolic pathways.
963 Relative abundance (%) of total modules within each GBM cluster (**B**). Relative abundance (%) of proteins encoded
964 by bins related to "Amino acid metabolism I" (**C**). Key pathways in amine metabolism within "Amino acid metabolism
965 I" (**D**). n = 11–13 per group. **E** Schematic of metabolic pathways annotated from whole-genome sequencing of PS128.
966 **F** Sankey diagram showing correlations between genes encoding enzymes involved in arginine, ornithine, and
967 spermidine/putrescine metabolism and bacterial strains enriched by PS128, together with the six most abundant
968 bacterial species. See also Fig. S4.
969
970

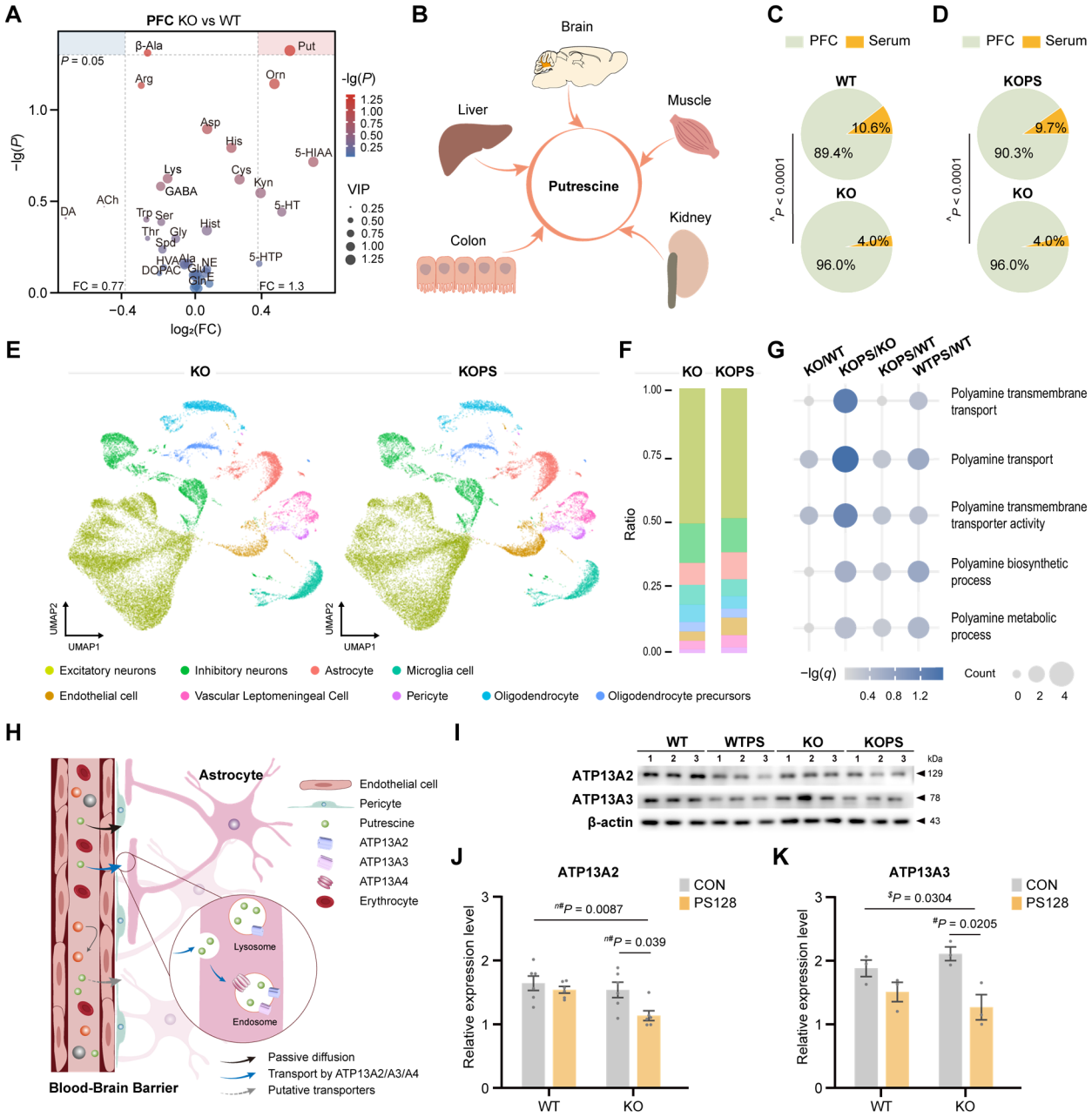

Fig. 5 Microbiota-targeted intervention rebalances peripheral–central putrescine homeostasis and transporter expression. A Differential metabolites in the PFC between KO and WT mice. Colors indicate -$\log_{10}$(P value), and bubble sizes represent variable importance in projection (VIP) scores. The x-axis denotes $\log_2$(fold change). n = 3 biological replicates, each pooled from six individuals (18 mice per group). FC, fold change. **B** Schematic illustrating major peripheral organs as sources of circulating putrescine. **C** and **D** Ratios of putrescine in the PFC relative to serum in WT versus KO mice (**C**) and in KOPS versus KO mice (**D**). n = 6 mice per group. **E** and **F** UMAP projection (**E**) and stacked bar plots (**F**) of cell-type composition derived from single-nucleus RNA sequencing (snRNA-seq) of PFC from 15-week-old mice. n = 2 biological replicates per group, each pooled from 3–4 individuals (7–8 mice per group). **G** Gene Ontology (GO) enrichment of differentially expressed genes (DEGs) in the PFC, highlighting pathways related to polyamine transport. -$\log_{10}$(q value) >1.3 was considered significant. Count, number of DEGs. DEGs were defined as $P < 0.05$ and $|\log_2$ fold change$| \geq 0.12$ with expression in at least 10% of PFC cells (Methods). **H** Schematic of two principal routes for putrescine transport. Putrescine crosses the blood–brain barrier (BBB) by passive diffusion or via active transport mediated by P5B-type ATPases (ATP13A2, ATP13A3, ATP13A4) and other putative

984 transporters. **I–K** Western blot of ATP13A2, ATP13A3, and β-actin in the PFC (**I**), with densitometric quantification
985 of ATP13A2 (**J**) and ATP13A3 (**K**) normalized to β-actin. n = 3–6 mice per group. Data are presented as mean ±
986 S.E.M. and gray dot represents individual mice. Statistical significance was determined using one-tailed ($^{\$}$) or two-
987 tailed ($^{\#}$) Student's t-test, or two-tailed ($^{n\#}$) Mann–Whitney U test as appropriate. A chi-square (^) test was used in (**C**
988 and **D**). A P value < 0.05 was considered significant. See also Figs. S5 and S6.

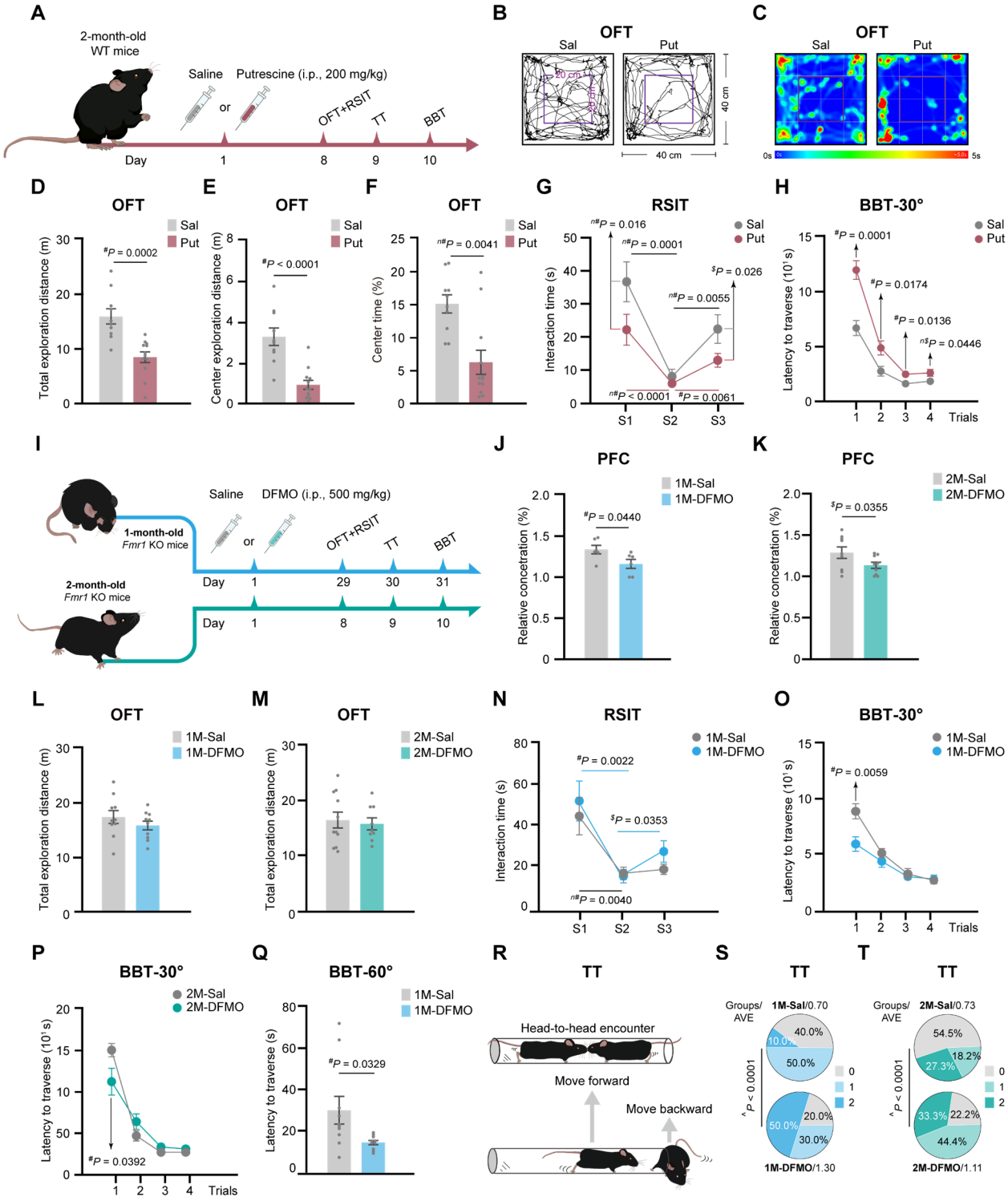

Fig. 6 Putrescine imbalance causally modulates autism-like behaviors in mice. A Schematic of putrescine intervention in 2-month-old WT mice and behavioral tests. i.p., intraperitoneal injection. **B–F** Representative traces (**B**) and heatmap (**C**) of the open-field test (OFT), total exploration distance (**D**), center exploration distance (**E**), and time spent in the center area (**F**). **G** Interaction time with familiar or novel mice across three stages of the reciprocal social interaction test (RSIT). S, stage. **H** Latency to traverse a 30° beam across four trials of the balance beam test (BBT). Effects of exogenous putrescine intervention in 2-month-old WT mice (**B–H**), n = 10–12. **I** Schematic of

DFMO intervention in 1- or 2-month-old *Fmr1* KO mice. i.p., intraperitoneal injection. **J** and **K** Relative putrescine concentration in the PFC after DFMO or saline injection from 1 month (**J**) or 2 months (**K**) of age, n = 6–9. **L** and **M** Total exploration distance in the OFT. **N** Interaction time with familiar or novel mice across three stages of the RSIT. **O–Q** Latency to traverse a 30° beam across four trials (**O** and **P**) or a 60° beam (**Q**) of the BBT. **R–T** Schematic of the tube test (TT) (**R**) and average score (AVE) per mouse obtained in the TT (**S** and **T**). Effects of endogenous putrescine inhibition by DFMO in 1- or 2-month-old *Fmr1* KO mice (**J–T**), n = 9–11. Data are presented as mean ± S.E.M. and gray dots indicate individual mice. One-tailed ($^{\$}$) or two-tailed ($^{\#}$) Student's t-test, one-tailed ($^{n\$}$) or two-tailed ($^{n\#}$) Mann–Whitney U test were used as appropriate. A chi-square (^) test was used in (**S** and **T**). A P value < 0.05 was considered significant. See also Fig. S7.

Graphical Abstract
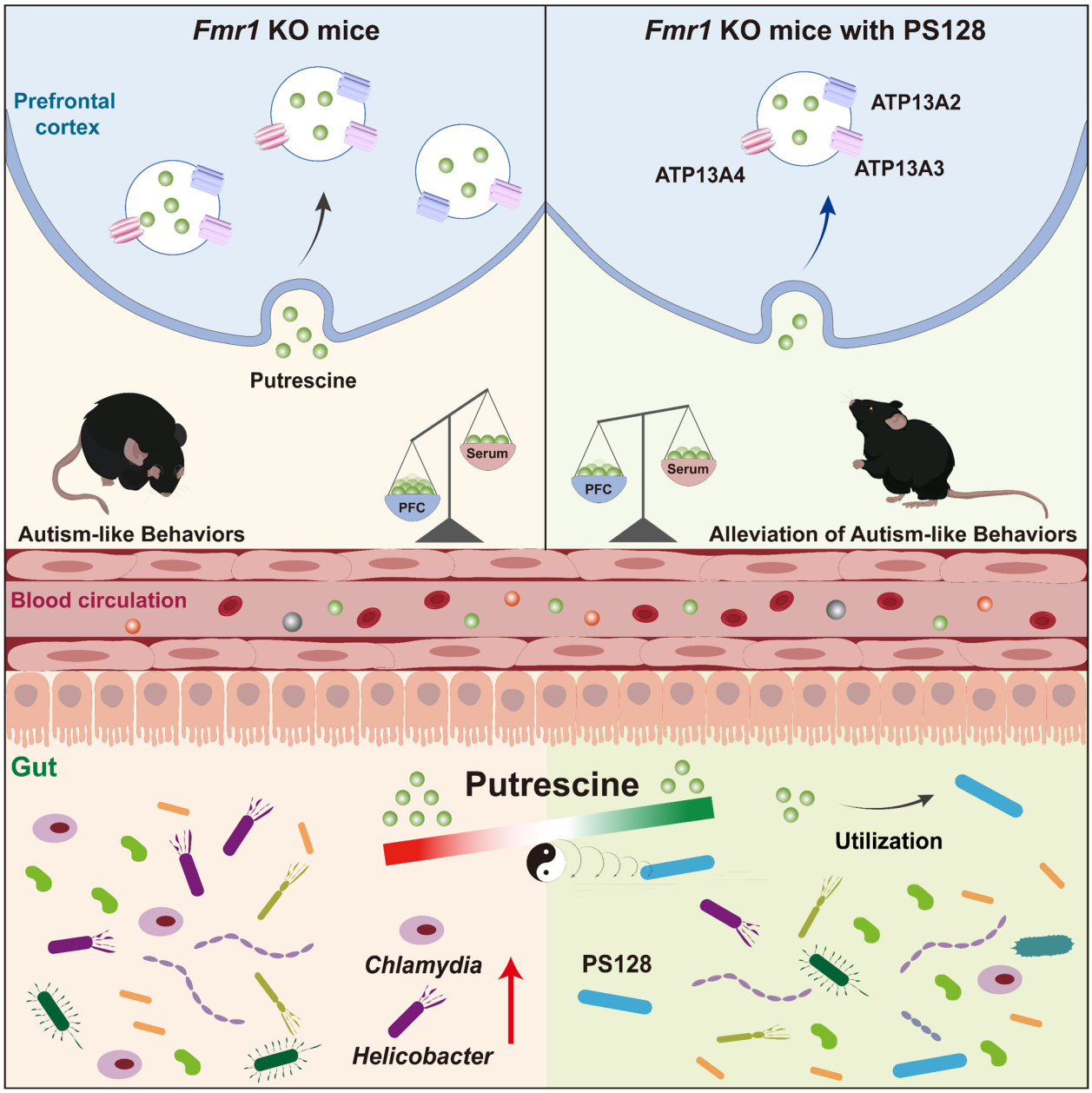
We identify dysregulated microbiota-driven polyamine homeostasis as a causal contributor to autism-like behaviors in *Fmr1* knockout mice. A psychobiotic intervention restores gut–brain metabolic balance and rescues social and repetitive behavioral deficits through coordinated microbial and host transport regulation.